5

Snow and Snowmelt

The goal of this chapter is to develop an understanding of the hydrologically important aspects of snow and snowmelt. We begin with an overview of the role of snow in the hydrologic cycle, then examine the nature of snow as a material, define critical snow properties, review techniques for measuring these properties, and survey the distribution of snow at local scales. The major focus of the chapter is a quantitative understanding of the processes that control the melting of snow (relying extensively on the physical principles discussed in chapter 3) and the movement of meltwater through the snowpack to the ground surface. This understanding is the basis for models used to predict and forecast snowmelt runoff, and we conclude with a review of approaches to snowmelt modeling.

5.1 Hydrologic Importance of Snow

Over much of the land above 45°N latitude (figure 2.26), a significant portion of precipitation falls as snow that is stored on the surface for periods ranging from hours to months before melting and continuing through the land phase of the hydrologic cycle. Figure 5.1 shows the steep latitudinal increase in the fraction of average annual precipitation falling as snow in North America; this fraction reaches about 65% on the north coast of Alaska (Dingman et al. 1980). Location relative to oceans and elevation also influence the portion of precipitation occurring as snow.

As noted by Frei et al. (2012), annual snow accumulation and melt are among the most dramatic environmental changes on the earth's surface. These phenomena influence a range of oceanographic, climatic, and ecological, as well as hydrologic, processes, including (1) the surface energy balance, (2) the stability of permafrost and consequent effects on global carbon budgets, and (3) fresh-water flux to the oceans and the strength of oceanic circulations.

In areas with a significant seasonal snowpack, it is the amount and timing of **water input** (i.e., snowmelt plus rain) rather than of precipitation, that largely determines the availability of water to vegetation and the amount and timing of streamflow (including floods) and ground-water recharge (figure 5.2 on p. 205). Since a smaller proportion of snowmelt than of rainfall is evaporated and transpired, snowfall contributes proportionally more to runoff and ground-water recharge; L'vovich (1974) estimated that more than half the annual runoff is derived from snowmelt in much of the Northern Hemisphere (figure 5.3 on p. 206). For mountain regions, as much as 85% of the annual runoff may come from snowmelt (Shafer and Dezman 1982).

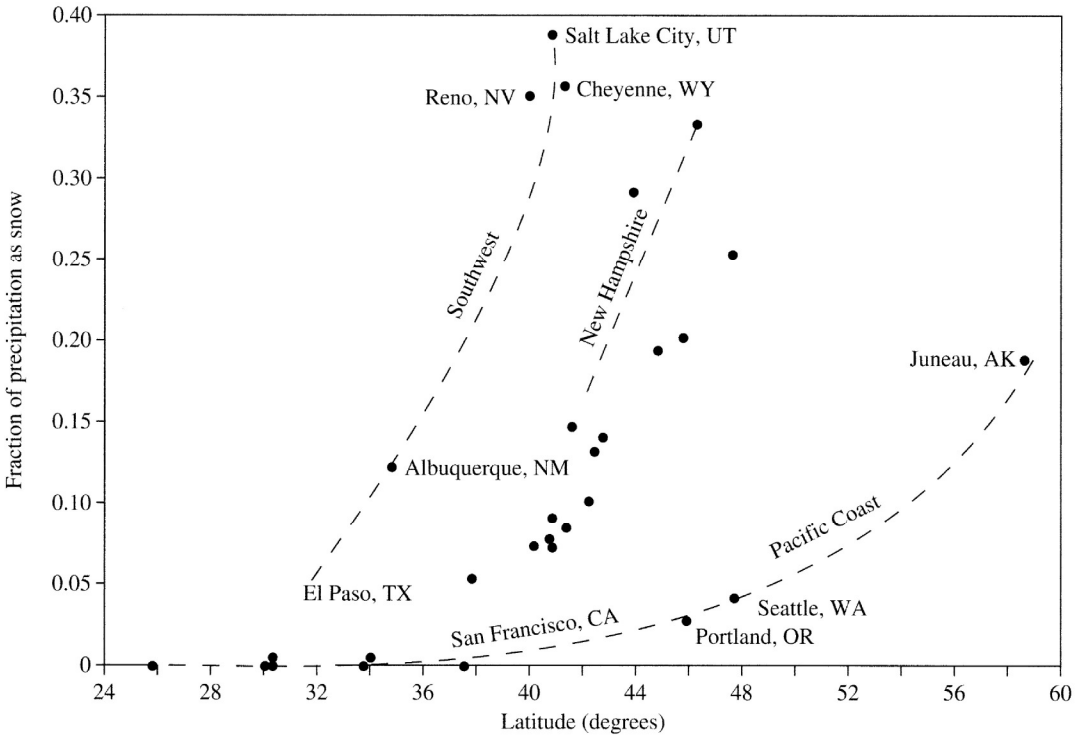

Figure 5.1
Fraction of precipitation occurring as snow as a function of latitude in the United States. City data from Todd (1970); unidentified points are for cities east of the Rocky Mountains. These fractions have probably decreased since these data were assembled due to warming (section 2.2.8.2).

In spite of the hydrologic importance of the melting of seasonal snow, there have been few studies characterizing water-input climatology. An early regional study showed that water-input climatology in New England is determined by latitude and elevation, and it developed a method for determining climatic and synoptic patterns of water input from standard network observations of temperature and precipitation (Hendrick and DeAngelis 1976). More recently, Bookhagen and Burbank (2010) quantified the hydrologic importance of snowmelt in the Himalayas, where changes in the timing or amount of snowmelt due to increasing temperatures or decreasing winter precipitation may have far-reaching societal consequences.

The overwhelming evidence of general global warming (section 2.1.3.2) makes a broader understanding of the role of snow in the hydrologic cycle of critical importance. To provide a general framework for this understanding, Molini et al. (2011) used a simple model of climate and watershed response to explore the relation between streamflow and water-input climatology. They found that, while increased air temperatures reduce winter snow accumulation and reduce total snowmelt amounts, they intensify snowmelt rate and thus increase the annual peak discharge. Thus there is an optimal warm-season length for which the annual peak discharge reaches a maximum; this length is a function of the watershed residence time[1] (figure 5.4 on p. 206). Where warm-season length is less than this optimum, peak discharge is limited by slow melting dynamics; where it is greater, peak discharge is reduced by decreased winter snow accumulation. Thus although global snow cover has been declining markedly over the last two decades and the average annual duration of Northern Hemisphere snow cover has decreased by 15 to 18 days since the early 1970s (box 2.3), the magnitudes of snowmelt floods could increase or decrease depending on warm-season length and watershed characteristics.

The dynamics of floods due to heavy rain and accompanying warm temperatures on an extensive snowpack ("rain-on-snow floods") are not well understood, and are likely to become an increasing hazard due to global warming, especially in Arctic regions (Putkonen et al. 2009). Jones and Perkins (2010) examined the effects of snow, event size, basin size, and forest harvest on floods in three small (< 1 km^2) and six large (60–600 km^2) watersheds in the western Cascades of Oregon. Rain-on-snow events delivered 75% more water to soils than rain events; peak discharges of rain-on-snow events were almost twice as high as rain-event peaks in large basins, but

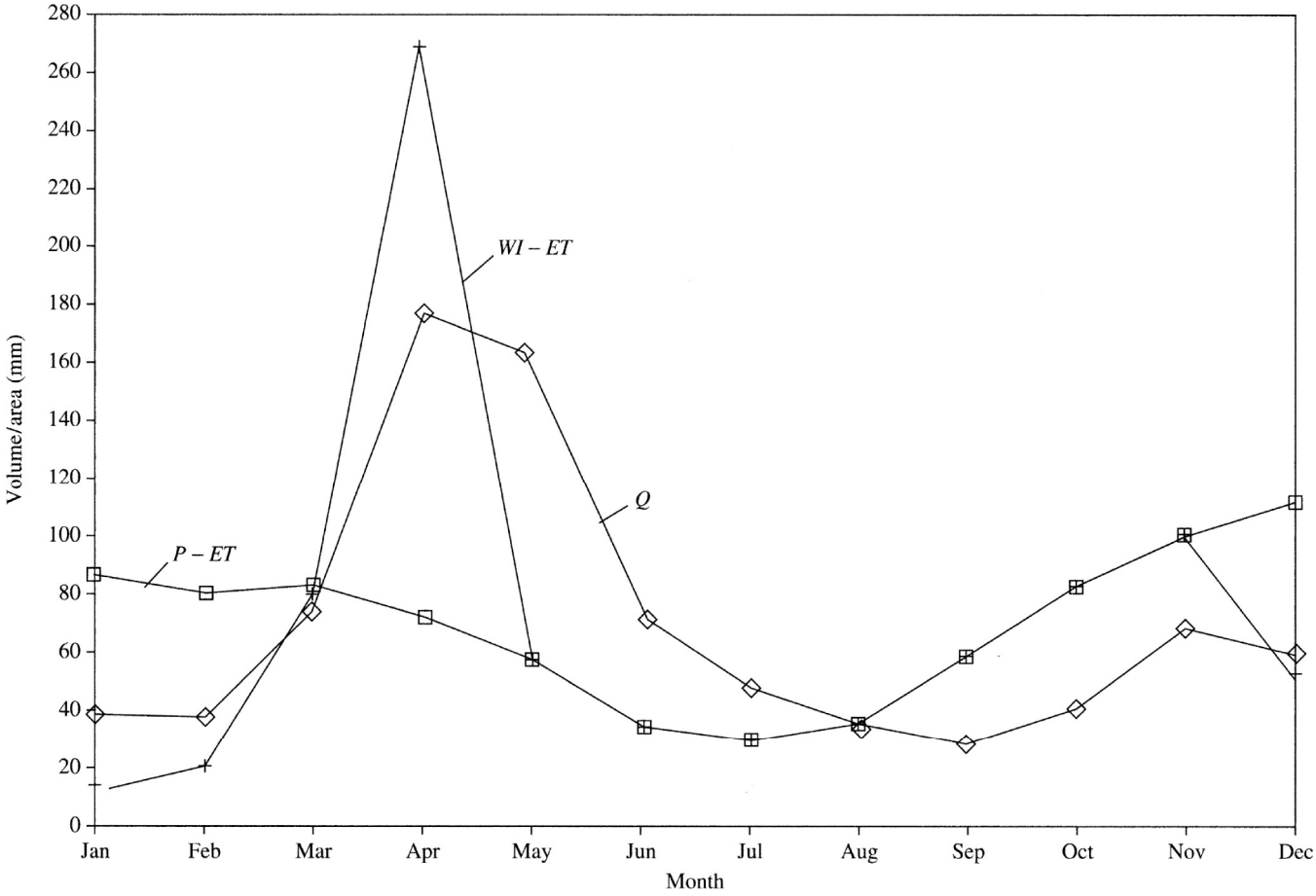

Figure 5.2 Average monthly precipitation minus evapotranspiration (*P – ET*) and water input (snowmelt plus rainfall) minus evapotranspiration (*WI – ET*) compared with streamflow (*Q*) in the Pemigewasset River basin, New Hampshire. The timing of streamflow is more closely related to *WI – ET* than to *P – ET*.

only slightly higher in small basins. In extreme floods, prolonged precipitation and synchronous snowmelt produced rapid, synchronized hydrograph responses to small variations in precipitation intensity. They found that the evolving structure of forests has an important influence on extreme rain-on-snow floods, and that further work is needed to delineate areas experiencing snowmelt and describe flow paths in melting snowpacks.

5.2 Material Characteristics of Snow

5.2.1 Snow Properties

Snow is a granular, porous medium consisting of ice and pore spaces. The size of a snow particle, *d*, is measured at its largest dimension (Colbeck et al. 1990) and covers the ranges shown in table 5.1 on p. 207. When snow is **cold** (i.e., its temperature is below the melting point of ice, 0°C), the pore spaces contain only air (including water vapor). At the melting point, the pore spaces can contain liquid water as well as air, and snow becomes a three-phase system.

Snow depth is the vertical distance from the ground surface to the snow surface. Using the symbols *M* to designate mass [M], *V* for volume [L^3], *h* for height [L], and ρ for mass density [$M\ L^{-3}$], and the subscripts *s* for snow, *i* for ice, *w* for liquid water, *swe* for water substance (water plus ice), and *a* for air, we consider a representative portion of a snowpack of surface area *A* (figure 5.5 on p. 208) and volume

$$V_s = V_i + V_w + V_a = h_s \cdot A \qquad \textbf{(5.1)}$$

to define quantities that characterize a snowpack:

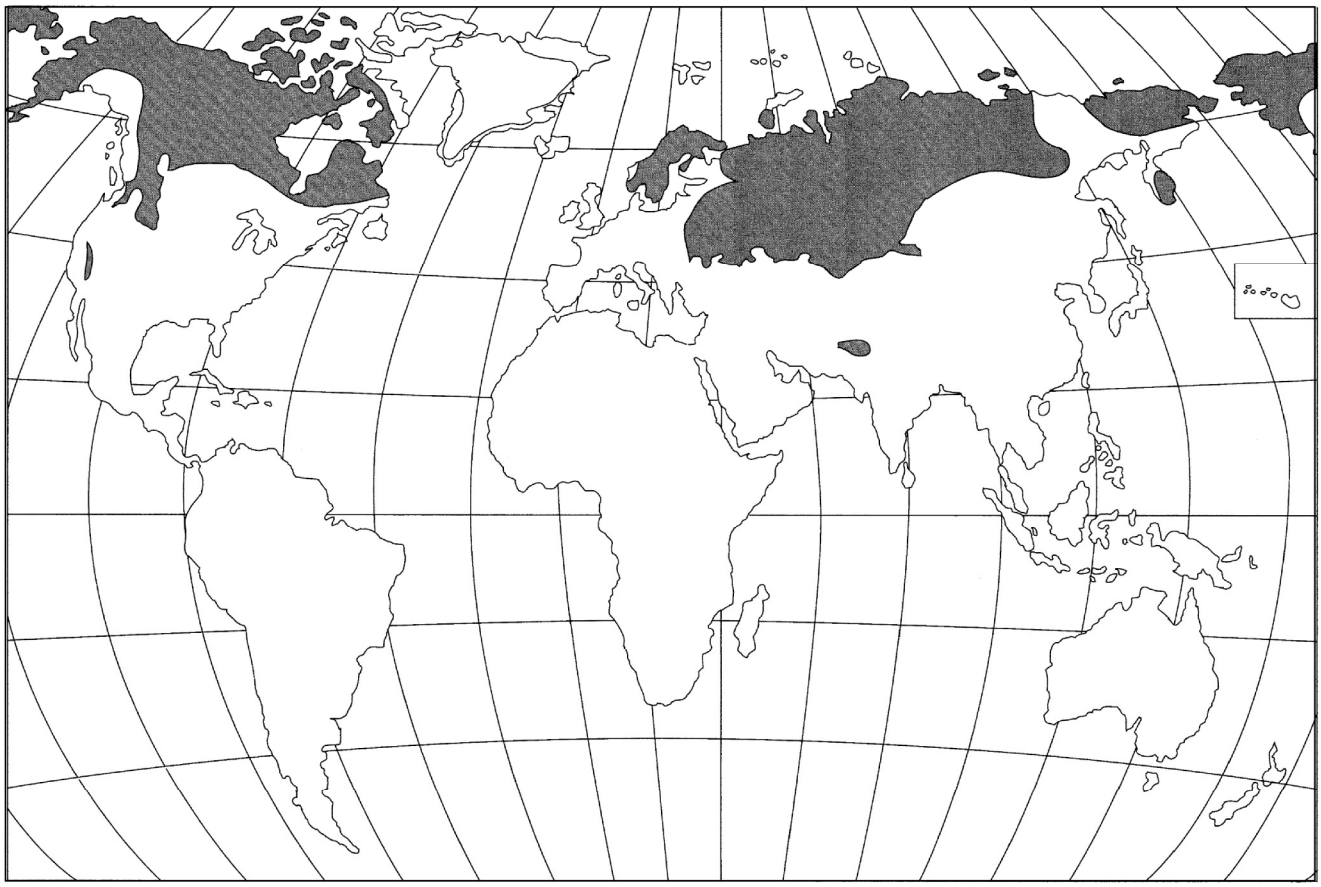

Figure 5.3 Regions in which more than half the annual runoff is derived from snowmelt [L'vovich (1974). *World Water Resources and Their Future*. Trans. by R. L. Nace, with permission of the American Geophysical Union].

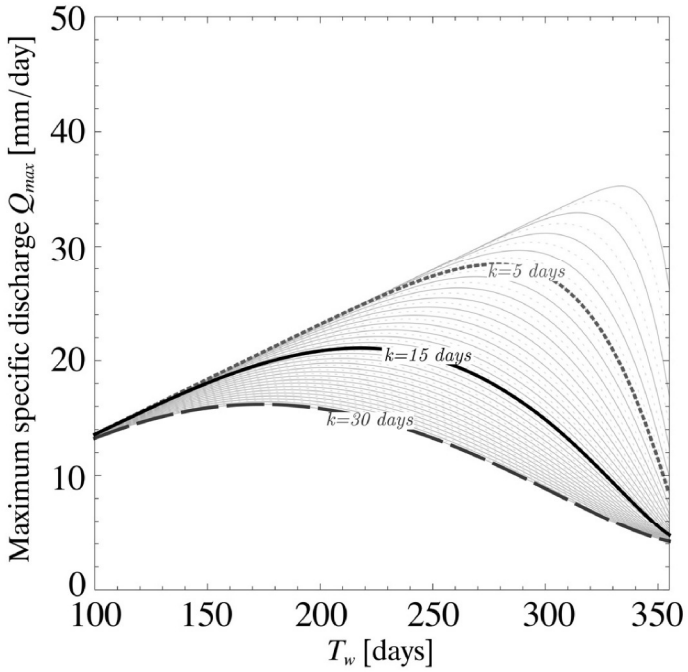

Figure 5.4 Peak discharge (Q_{max}) as a function of melting-season duration, T_w, and basin residence time, k, as modeled by Molini et al. (2011) (Maximum discharge from snowmelt in a changing climate. *Geophysical Research Letters* 38, with permission of the American Geophysical Union).

- **Porosity** (ratio of pore volume to total volume)

$$\phi \equiv \frac{V_w + V_a}{V_s}; \qquad \textbf{(5.2)}$$

- **Snow density** (mass per unit volume of snow)

$$\rho_s = \frac{M_i + M_w}{V_s} = \frac{\rho_i \cdot V_i + \rho_w \cdot V_w}{V_s}; \qquad \textbf{(5.3)}$$

- **Liquid-water content** (ratio of liquid-water volume to total snow volume)

$$\theta_w \equiv \frac{V_w}{V_s}. \qquad \textbf{(5.4)}$$

Table 5.1 shows the ranges of snowpack liquid-water contents.

Table 5.1 Snow Properties.

(A) Grain Size (*d*)

Term	*d* (mm)
Very fine	< 0.2
Fine	0.2 to 0.5
Medium	0.5 to 1.0
Coarse	1.0 to 2.0
Very coarse	2.0 to 5.0
Extreme	> 5.0

Source: Colbeck et al. (1990).

(B) Liquid-Water Content (θ_w)

Term	Description[a]	Range of θ_w
Dry	$T_s < 0$ usually, but can occur at $T_s = 0$. Snow grains have little tendency to stick together when pressed.	0
Moist	$T_s = 0$. Water not visible even at 10× magnification. Snow grains tend to adhere when lightly crushed.	< 0.03
Wet	$T_s = 0$. Water visible as inter-grain menisci at 10× magnification, but cannot be squeezed out.	0.03 to 0.08
Very wet	$T_s = 0$. Water can be squeezed out by moderate pressing, but significant air spaces present.	0.08 to 0.15
Slush	$T_s = 0$. Snow flooded with water, few air spaces.	> 0.15

[a] T_s = snowpack temperature (°C)

Source: Colbeck et al. (1990).

(C) Field Estimation of Snowpack Density (ρ_s)

Observation	Density (kg/m^3)
Supports an adult without skis.	320 to 350
Foot leaves only a slight impression.	350 to 380
Foot leaves no mark on the surface.	> 400

Source: Rikhter (1954).

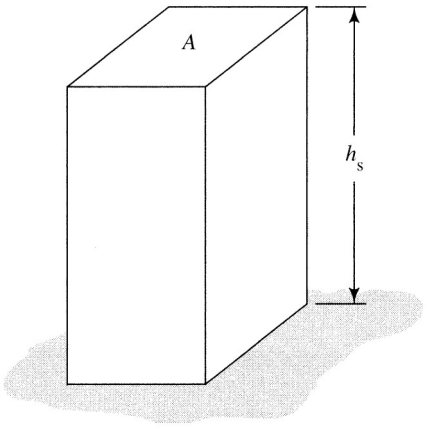

Figure 5.5 Dimensions of a representative portion of a snowpack used in defining snowpack properties. *A* is the area of the upper surface, h_s is the snow depth.

Combining equations (5.2)–(5.4) allows us to relate snow density, liquid-water content, and porosity as

$$\rho_s = (1-\phi)\cdot\rho_i + \theta_w\cdot\rho_w, \qquad \textbf{(5.5)}$$

where $\rho_i = 917$ kg/m^3 and $\rho_w = 1{,}000$ kg/m^3 (at 0°C).

For the hydrologist, the most important property of a snowpack is the amount of water substance it contains, i.e., the depth of water that would result from the complete melting of the snow in place.

This is the **snow-water equivalent** (**SWE**) of the snowpack, h_{swe}:

$$h_{swe} \equiv \frac{V_w + V_i\cdot(\rho_i/\rho_w)}{A}. \qquad \textbf{(5.6)}$$

Noting that

$$V_i = (1-\phi)\cdot V_s, \qquad \textbf{(5.7)}$$

and substituting equations (5.4) and (5.7), equation (5.6) becomes

$$V_{swe} = \theta_w\cdot V_s + (1-\phi)\cdot V_s\cdot\frac{\rho_i}{\rho_w}. \qquad \textbf{(5.8)}$$

We can now utilize equations (5.1) and (5.6) to rewrite equation (5.8) as

$$\begin{aligned} h_{swe} &= \theta_w\cdot h_s + (1-\phi)\cdot h_s\cdot\frac{\rho_i}{\rho_w} \\ &= \left[\theta_w + (1-\phi)\cdot\frac{\rho_i}{\rho_w}\right]\cdot h_s. \end{aligned} \qquad \textbf{(5.9)}$$

Finally, we see from equation (5.5) that equation (5.9) can be written as

$$h_{swe} = \frac{\rho_s}{\rho_w}\cdot h_s. \qquad \textbf{(5.10)}$$

In words, equation (5.10) is expressed as

"water equivalent equals density times depth,"

where density is understood to mean *relative* density (i.e., specific gravity).

5.2.2 Snowpack Metamorphism

The density of new-fallen snow is determined by the configuration of the snowflakes, which is largely a function of air temperature, the degree of supersaturation in the precipitating cloud, and the wind speed at the surface of deposition (Mellor 1964). Higher wind speeds tend to break snowflakes that formed in stellar or needle-like shapes and to pack them together into denser layers. Observed relative densities (ρ_s/ρ_w) of freshly fallen snow range from 0.004 to 0.34 (McKay 1970), with the lower values occurring under calm, very cold conditions and higher values accompanying higher winds and higher temperatures; the usual range is $0.07 \le \rho_s/\rho_w \le 0.15$ (Garstka 1964).

Because of the difficulty in measuring the density of new snow,

an average relative density of 0.1 is often assumed to apply when converting snowfall observations to SWE.

However, the user of water-equivalent data should be aware of the potential for significant errors in estimates based on an assumed density (Goodison et al. 1981). New-snow density (kg/m^3) can be estimated as a function of wet-bulb temperature, T_{wb}, as

$$\rho_s = 50 + 1.7\cdot(T_{wb} + 15)^{1.5} \qquad \textbf{(5.11)}$$

(Melloh et al. 2002), where

$$T_{wb} \approx (2\cdot T_a + T_{dp})/3;\ 0 \le T_a \le 10°\text{C}, \qquad \textbf{(5.12)}$$

T_a is air temperature (°C), and T_{dp} is dew-point temperature (°C) (section 3.2.5).

As soon as snow accumulates on the surface it begins a process of metamorphism that continues

until melting is complete. Four mechanisms are largely responsible for this process: (1) gravitational settling; (2) destructive metamorphism; (3) constructive metamorphism; and (4) melt metamorphism.

Gravitational settling in a given snow layer takes place at rates that increase with the weight of the overlying snow and the temperature of the layer and decrease with the density of the layer. According to relations given by Anderson (1976), one can expect gravitational settling to increase density at rates on the order of 2 to 50 $kg/m^3 \cdot d$ in shallow snowpacks. On glaciers, the pressure of thick layers of accumulating snow is the principal factor leading to the formation of solid ice.

Destructive metamorphism occurs because vapor pressures are higher over convex ice surfaces with smaller radii of curvature, so the points and projections of snowflakes tend to evaporate (sublimate) and the vapor to redeposit on nearby, less convex surfaces. This leads to the formation of larger, more spherical snow grains with time. This process is primarily important in snowflakes that have recently fallen, causing the density of a new-snow layer to increase at about 1% per hour. The process ceases to be important when densities reach about 250 kg/m^3 (Anderson 1976).

Constructive metamorphism is the most important pre-melt densification process in seasonal snowpacks. Over short distances, this process occurs by **sintering**, in which water molecules are deposited in concavities where two snow grains touch, gradually building a "neck" between adjacent grains. Over longer distances, constructive metamorphism can occur as a result of vapor transfer within a snowpack due to temperature gradients; sublimation occurs in warmer portions of the snowpack and the water vapor moves toward colder portions where condensation occurs. Very cold air overlying a relatively shallow snowpack often produces a strong upward-decreasing temperature gradient within the snow, with a concomitant upward-decreasing vapor-pressure gradient. Under these conditions, snow near the base of the pack evaporates at a high rate, often resulting in a basal layer of characteristic large planar crystals with very low density and strength called **depth hoar**.

Melt metamorphism occurs via two processes. In the first, liquid water formed by melting at the surface or introduced as rain freezes as it percolates downward into the cold snowpack. This results in densification, and may produce layers of essentially solid ice that extend over long distances. The freezing at depth also liberates latent heat, which contributes to the warming of the snowpack and the acceleration of vapor transfer. The second metamorphic process accompanying melt is the rapid disappearance of smaller snow grains and growth of larger grains that occurs in the presence of liquid water. Because of this phenomenon, an actively melting snowpack is typically an aggregation of rounded grains the size of coarse sand (1 to 2 mm diameter) (Colbeck 1978).

Except for the temporary formation of depth hoar, all the processes of metamorphism lead to a progressive increase in density throughout the snow-accumulation season (figure 5.6). It should be noted, however, that there is much year-to-year variability in snowpack characteristics and that both snowfall and the processes causing metamorphism occur at highly variable rates over short distances due largely to differences in slope, aspect, and vegetative cover.

At the beginning of the melt season, the snowpack is typically vertically heterogeneous as well, with perhaps several layers of markedly contrasting grain sizes and densities. During melt, density continues to increase and the vertical inhomogeneities tend to disappear. During this period, density can fluctuate on an hourly or daily time scale due to the formation and drainage of meltwater. Snowpacks that are at 0°C and well drained tend to have relative densities near 0.35 (McKay 1970).

5.3 Measurement of Snow and Snowmelt

Discussion of measurement of snow and snowmelt requires definition of several terms:

- **Precipitation** is the incremental *water-equivalent depth* of rainfall, snow, sleet, and hail falling during a given storm or measurement period.
- **Snowfall** is the incremental *depth* of snow and other forms of solid precipitation that accumulates on the surface during a given storm or measurement period.
- **Snowpack** is the accumulated snow on the ground at a time of measurement. Its *water-equivalent depth* (h_{swe}) (SWE) is of particular hydrologic interest; its depth (h_s) and density (ρ_s or ρ_s/ρ_w) are also measured.
- **Snow cover** is the *areal extent* of snow-covered land surface. It may be measured in absolute terms [L^2] or as a fraction of a particular area.

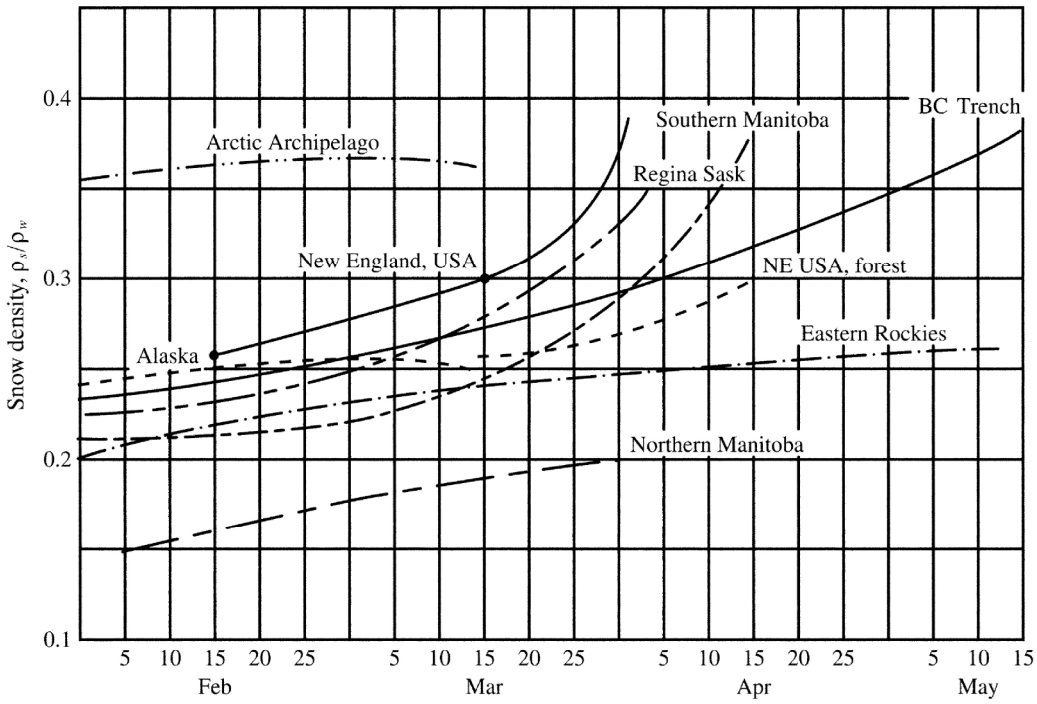

Figure 5.6
Seasonal variation in snowpack relative densities in various regions of North America [adapted from McKay (1970)].

- **Ablation** is the incremental *water-equivalent depth* (volume per unit area) that leaves the snowpack during a given time period. It is the sum of snowmelt plus evaporation/sublimation.
- **Snowmelt** is the incremental *water-equivalent depth* (volume per unit area) that is produced by melting and leaves the snowpack during a given time period.
- **Water output** is the incremental *water-equivalent depth* (volume per unit area) that leaves the snowpack during a given time period. It is the sum of rain plus snowmelt that has percolated through the snowpack.

Approaches to measurement of each of the quantities listed above are discussed below and summarized in table 5.2. Sources of snow data are listed in box 5.1.

5.3.1 Precipitation

5.3.1.1 Standard Gauges

As discussed in section 4.2.1.1, standard network measurements of precipitation are made via collecting gauges that weigh the total in-falling water substance or melt the snow and ice that is collected. In most cases, the form of the precipitation is not recorded. As noted in section 4.2.1.2, measurements in such gauges are subject to several sources of error, the most important of which is due to wind, and

Box 5.1 Snow-Data Sources

- Monthly reports and maps of Northern Hemisphere snow-cover extent are available at http://www.ncdc.noaa.gov/sotc/global-snow http://earthobservatory.nasa.gov/GlobalMaps/view.php?d1=MOD10C1_M_SNOW
- Daily, weekly, and monthly maps of Northern Hemisphere snow-cover extent and maps of monthly snow-cover climatology are available at http://climate.rutgers.edu/snowcover/
- Daily maps of snow cover for the United States and the Northern Hemisphere are available at http://www.nohrsc.noaa.gov/nh_snowcover/
- Preliminary daily snowfall and snow-depth observations collected from NWS Cooperative Observer Program stations and NWS First Order stations can be found at http://www.ncdc.noaa.gov/snow-and-ice/dly-data.php
- Current SNOTEL data and maps are available at http://www.wrcc.dri.edu/snotel.html

Table 5.2 Methods of Measuring Depth, Water Equivalent, and Areal Extent of Precipitation, Snowfall, Snowpack, and Snowmelt.

Parameter	Depth	Water Equivalent	Areal Extent
Precipitation		Standard storage gauges (G) Universal gauge (G)	Gauge networks (G) Radar (G, S)
Snowfall	Ruler and board (G)	Melt snow on board (G) Use estimated density (G) Universal gauge (G) Snow pillow (G)	Observation networks (G) Radar (G, S) Visible/infrared (S)
Snowpack	Snow stake (G, A) Snow tube (G) Ultrasonic gauge (G) GPS receivers (S)	Universal gauge (G) Snow tube (G) Snow pillow (G) Radioisotope gauge (G) Natural gamma radiation (G, A) Microwave (A, S) GRACE[a] (S)	Snow surveys (G) Aerial observation (A) Visible/infrared (S) Microwave (A, S)
Snowmelt and water output		Snow pillow (G) Lysimeter (G) Universal gauge (G)	Snow-pillow network (G)

A = airborne
G = ground-based
S = satellite-borne
[a] GRACE = Gravity Recovery and Climate Experiment

gauge-catch deficiencies are especially large for snow (figure 4.22). A World Meteorological Organization (WMO) study (Goodison et al. 1998) compared gauge-catch deficiencies for snow and mixed precipitation of the standard gauges used in 16 countries; the standard was a Tretyakov gauge (figure 4.18) surrounded by bushes at the same height. The results, summarized in table 5.3 and figure 5.7, show that standard network precipitation-gauge measurements must be significantly adjusted for wind in periods in which snow is important (Legates and DeLiberty 1993; Yang et al. 1998). In the extreme cold of the high Arctic and high elevations, where snow particles are small and subject to especially high winds, gauge-catch deficiencies are even greater than those found in the WMO study (Sugiura et al. 2006).

5.3.1.2 Universal Gauges

Cox (1971) developed a "universal surface precipitation gauge" that measures all the quantities listed in table 5.2 simultaneously. Waring and Jones (1980) modified Cox's design to make it more suitable for shallow snowpacks (figure 5.8 on p. 213). This gauge measures snowfall and SWE by weight and collects and measures water output. An increase in the weight recorded by a snow pillow (see below) would usually indicate a snowfall event, although rainfall that stayed in the snowpack would also cause a weight increase. Clearly the installation of these gauges is considerably more elaborate and expensive than that of standard gauges, and they have not been widely used in observation networks.

Recently, several commercial companies have developed "universal precipitation gauges" that are designed to accurately measure the water equivalent of snowfall as well as rain, but are less elaborate than the installation shown in figure 5.8. Many of these are precipitation collectors with aerodynamic designs and are heated for snow collection. These instruments may provide improved gauge-catches in windy conditions, but are not in wide network use. Information about various designs can be found by searching the Internet for "universal precipitation gauges."

5.3.1.3 Radar

The use of radar in precipitation measurement was described in section 4.2.2. Although it provides spatially continuous observations at small time intervals, it measures falling precipitation rather than that reaching the ground, and the single-polarization sys-

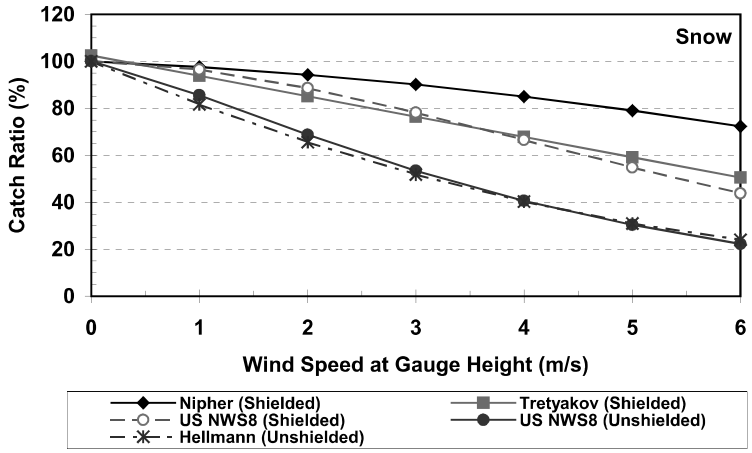

Figure 5.7 Average catch ratios for snow measured for five gauge types [Goodison et al. (1998). *WMO Solid Precipitation Measurement Intercomparison Final Report*. WMO/TD No. 872, courtesy of World Meteorological Organization)].

Table 5.3 Catch Ratios as a Function of Gauge-Height Wind Speed and Air Temperature for Standard Precipitation Gauges.

(A) Snow

Gauge Type	Used in	Equation	*n*	r^2	Standard Error (%)[a]
Nipher shielded	Canada	$R = 100 - 0.44 \cdot u(z_g)^2 - 1.98 \cdot u(z_g)$	241	0.40	11.05
Tretyakov	Russia	$R = 103.11 - 8.67 \cdot u(z_g) + 0.30 \cdot T_{max}$	381	0.66	10.84
US 8-in shielded	United States	$R = \exp[4.61 - 0.04 \cdot u(z_g)^{1.75}]$	107	0.72	9.77
US 8-in unshielded	United States	$R = \exp[4.61 - 0.16 \cdot u(z_g)^{1.28}]$	55	0.77	9.41
Hellmann unshielded	Germany, Denmark, Croatia	$R = 100 - 1.13 \cdot u(z_g)^2 - 19.45 \cdot u(z_g)$	172	0.75	11.97

(B) Mixed Precipitation

Gauge Type	Used in	Equation	*n*	r^2	Standard Error (%)[a]
Nipher shielded	Canada	$R = 97.29 - 3.18 \cdot u(z_g) + 0.58 \cdot T_{max} - 0.67 \cdot T_{min}$	177	0.38	8.02
Tretyakov	Russia	$R = 96.99 - 4.46 \cdot u(z_g) + 0.88 \cdot T_{max} + 0.22 \cdot T_{min}$	433	0.46	9.15
US 8-in shielded	United States	$R = 101.04 - 5.62 \cdot u(z_g)$	75	0.59	7.56
US 8-in unshielded	United States	$R = 100.77 - 8.34 \cdot u(z_g)$	59	0.37	13.66
Hellmann unshielded	Germany, Denmark, Croatia	$R = 96.63 + 0.41 \cdot u(z_g)^2 - 9.84 \cdot u(z_g) + 5.95 \cdot T_{avg}$	285	0.48	15.14

$R \equiv$ gauge-catch ratio (%)
$u(z_g) \equiv$ wind speed at gauge height (m/s)
$T_{max} \equiv$ maximum air temperature (°C)
$T_{min} \equiv$ minimum air temperature (°C)
$T_{avg} \equiv$ average air temperature (°C)
$n \equiv$ number of observations
$r \equiv$ correlation coefficient (see section C.4)

[a] 95% of observed R values are within 2 standard errors of the value given by the equation.

Source: Goodison et al. (1998).

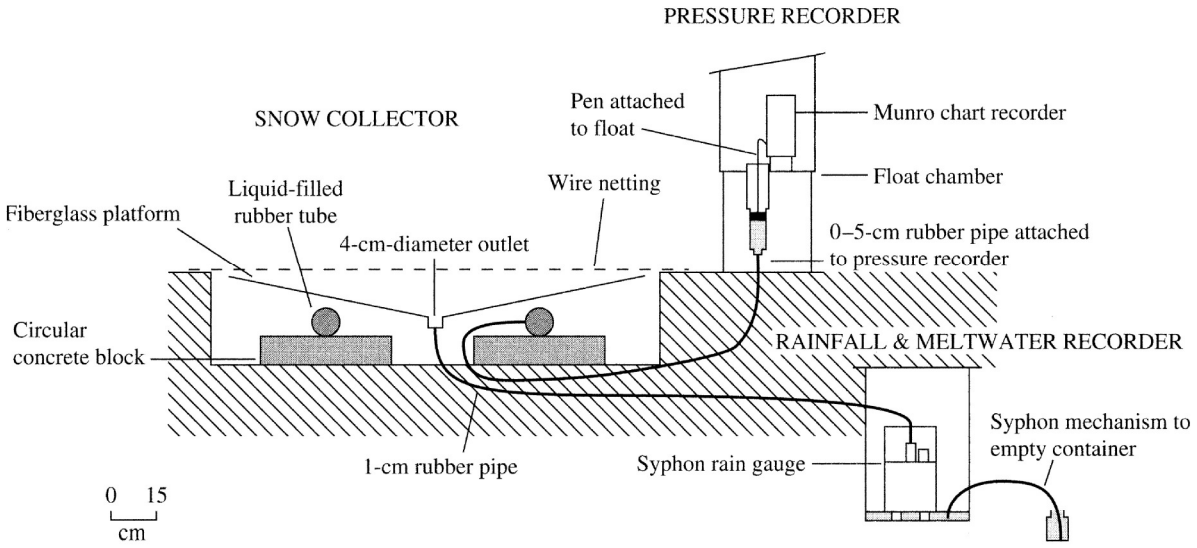

Figure 5.8 Diagram of the universal gauge, which can measure precipitation, snowfall, water equivalent, and water output [Waring and Jones (1980). A snowmelt and water equivalent gauge for British conditions. *Hydrological Sciences Bulletin* 25:129–134, courtesy of International Association of Hydrological Sciences].

tems currently used cannot reliably separate rain from snow. Dual-polarization systems, which are now being integrated into radar networks, will provide improved detection of snow.

5.3.2 Snowfall

5.3.2.1 Rulers

Snowfall is usually measured simply by a ruler placed vertically on a board that was set on the previous snow surface.

5.3.2.2 Ultrasonic Sensors

Ultrasonic snow-depth sensors measure the time for high-frequency (50 kHz) sound waves to travel and return from a source mounted above the snow to the snow surface. Air temperature is monitored, and the time is converted to a distance by multiplying distance by the temperature-adjusted sound velocity. Tests have shown that this technology is a practical and reliable means of obtaining snow-fall and snow-depth information from remote locations (Chow 1992; Ryan et al. 2008; Rice and Bales 2010).

5.3.3 Snowpack and Snow Cover

5.3.3.1 Snow Stakes

The depth of snow cover can be simply observed by inserting a ruler through the snow to the ground surface, or by observing the height of the snow surface against a fixed ruler, called a **snow stake**, with its zero point at the ground surface. In some remote areas, permanent snow stakes are designed with large markings so that readings can be made from aircraft.

5.3.3.2 Ultrasonic Sensors

The ultrasonic snow-depth sensors described in section 5.3.2.2 provide generally reliable monitoring of snowpack depth.

5.3.3.3 Snow Surveys

As noted, the most important snow information for the hydrologist is the water equivalent of the snow cover. Network measurements of this quantity are most commonly obtained via periodic **snow surveys** at fixed locations called **snow courses**, coupled with automated snow-pillow stations (section 5.3.3.4).

A snow course is a path between two fixed end points over which a series of measurements of snow depth and SWE are made. The length of the path is typically 150 to 250 m, with measurements made at about six points (more if snow conditions are highly variable) spaced at a fixed interval of at least 30 m. At each point, a coring tube equipped with a toothed cutting rim, called a **snow tube** (figure 5.9), is inserted vertically to the surface. After the snow depth is read against markings on the outside of the tube, the tube is pushed a few centimeters into the soil and twisted to secure a small plug of soil that retains the snow in the tube. The tube is then extracted and weighed on a specially calibrated scale that is pre-tared and reads

directly in centimeters or inches of water equivalent. Density at each point can be calculated via equation (5.10), and SWE for the course is the average of the values at the measurement points. A detailed guide for snow-survey techniques was published by the US Soil Conservation Service (1984) and can be accessed at http://www.wcc.nrcs.usda.gov/factpub/ah169/ah169.htm.

Several different designs of snow tube are available; they may be made of aluminum or fiberglass and range in diameter from 3.8 to 7.6 cm. Comparisons with snow carefully excavated and weighed have shown a tendency for snow tubes to overestimate SWE by up to 10% (Work et al. 1965; Goodison et al. 1981).

In shallow (i.e., less than about 1 m) snowpacks, depth and density have been found to be essentially independent, and there is typically less temporal and spatial variability in density than in depth (Goodison et al. 1981). Under these conditions, little precision is lost and considerable time may be gained by making more depth measurements than SWE measurements (Jonas et al. 2009).

A snow-course network, like a precipitation-gauge network, should be designed to provide a representative picture of the snowpack in the region of interest. However, since measurements are labor intensive, snow courses are usually considerably more widely spaced than gauges and are usually read at longer time intervals—e.g., every two weeks during the snow season. Because snowpack conditions are largely determined by local conditions, snow-course networks should be designed to sample representative ranges of land use (vegetative cover), slope, aspect, and elevation. Areal averages may then be estimated by extrapolating from these measurements on the basis of the distribution of the various conditions in the region of interest. For operational purposes such as forecasting runoff, measurement agencies commonly rely on only a few snow-course sites that have been calibrated over a period of years to provide an index, rather than a sample estimate, of the watershed snow cover.

5.3.3.4 Snow Pillows

The water equivalent of snow cover can also be measured with **snow pillows**, which are circular or octagonal membranes made of rubber or flexible metal and contain a liquid with a low freezing point (figure 5.10). The weight of the snow on the pillow controls the pressure of the liquid, which is recorded or monitored via a manometer or pressure transducer.

The diameter of snow pillows ranges from 1 to 4 m, with larger diameters recommended for deeper snowpacks (Barton 1974). Several factors influence the accuracy and continuity of readings, including (1) leaks; (2) temperature variations that affect the density of the liquid; (3) the formation of ice layers within the snowpack, which can support a portion of the snow and lead to undermeasurement of SWE (called "bridging"); (4) disruption of the contact between the snow and the ground, which can distort the snowpack energy and water balances; and, in remote installations, (5) instability of power supply to sensors and recorders. Detailed considerations for installation and maintenance of snow pillows were given by Davis (1973) and Cox et al. (1978), and measurement problems were discussed by McGurk and Azuma (1992) and McGurk et al. (1993). If read frequently enough, snow pillows can be used to measure the water equivalent of individual snowfalls.

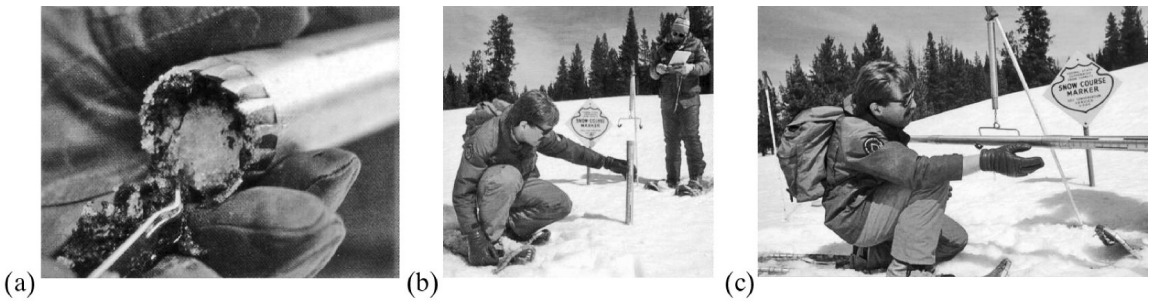

Figure 5.9 Measuring snow depth and water equivalent via a snow tube. (a) Teeth for securing a soil plug at the base of the snow tube. (b) Snow tube is pushed through snowpack to ground to measure depth and capture core. (c) Water equivalent is determined by weighing the tube and snow and subtracting the weight of tube (US Natural Resources Conservation Service, n.d.).

Figure 5.10 A snow pillow (foreground) and a water-output lysimeter (background) installed at the US National Weather Service snow-research site at Danville, Vermont. Buried lines transmit the fluid pressure from the pillow to a sensor, and the water released by the snowpack to a measuring device, both of which are in an instrument shelter. The metal ring is electrically heated, and is melted down through the snowpack to isolate the cylinder of snow above the lysimeter (photo by author).

The universal gauge (figure 5.8) measures SWE using the same basic principle as the snow pillow.

Snow pillows are well suited for remote installation. Since 1980, in the United States the NRCS has operated the SNOTEL network in 12 western states and Alaska, which consists of over 600 remotely located snow pillows that provide data on SWE with an accuracy of about 2.5 mm (Schaefer and Werner 1996), along with storage precipitation gauges and air-temperature recorders. Data are recorded every 15 minutes and reported daily via meteor-burst radio communications technology. The current generation of remote sites, master stations, and central computer facilities allows for hourly interrogation. Sites are battery powered with solar-cell recharge, and are designed to operate unattended and without maintenance for a year.

5.3.3.5 Self-Recording Ground-Temperature Sensors

Lundquist and Lott (2008) showed that small, inexpensive self-recording temperature sensors can be used to monitor spatial and temporal patterns of snow accumulation and melt in complex environments. The sensors are buried slightly below the soil surface, and provide a record of the presence or absence of snow cover, which can be detected because near-surface soil temperatures only experience diurnal temperature oscillations when they are not covered by an insulating layer of snow. When combined with an air temperature record and snowmelt model, the date snow cover disappears can be used to estimate the amount of snow that accumulated at the start of the melt season.

5.3.3.6 Radioactive Gauges

Several types of instruments exploiting the attenuation of gamma rays or neutrons by water substance can be used for nondestructive measurement of SWE. One version involves an artificial gamma-ray source (^{60}Co or ^{137}Cs) and a detector, one of which is at the ground surface with the other suspended above; the readings from the detector are typically transmitted by telemetry from a remote location to the observer. Bland et al. (1997) reported a method by which a portable gamma-ray source is inserted into permanent structures in the field at the time of measurement, and a handheld detector is

used to make a nondestructive determination of SWE with a precision of 3 mm.

For snowpacks with SWE less than about 40 cm, it is also possible to measure the attenuation by snow of natural gamma radiation emitted from the soil surface using a detector that is either fixed a few meters above the surface (Bissell and Peck 1973) or mounted on an aircraft (Loijens and Grasty 1973). Use of an airborne detector requires low-altitude (< 150 m) flights following a route over which the snow-free gamma emission has been previously determined; corrections for soil moisture and radioactive emissions can then be made from the air (Goodison et al. 1981; Foster et al. 1987). However, work by Grasty (1979) suggested that a simpler single-flight technique can give results of high accuracy. Carroll and Voss (1984) found good correlation between SWE determined from airborne gamma-radiation sensors and snow tubes in forested regions of the northern United States and Canada (figure 5.11a), as did Bergstrom and Brandt (1985) in Sweden. The NWS Airborne Snow Survey Program (http://www.nohrsc.noaa.gov/snowsurvey) uses low-flying aircraft to estimate SWE via natural gamma radiation (Carroll and Carroll 1989).

5.3.3.7 Airborne Microwave and Radar

Microwave radiation (wavelengths of 0.1 to 50 cm), including radar, can be used to remotely measure SWE, areal extent, and other properties of snow cover. Airborne systems exploiting these wavelengths have the advantage of being able to "see through" clouds; however, some of the many variables that affect the observations and methods for interpreting data are still being worked out.

The flux of microwave radiation emitted by a snowpack depends on its density, temperature, grain size, and the underlying soil conditions. Thus considerable information about ground conditions is required for translating "passive" microwave emissions to estimates of SWE (Foster et al. 1987).

Radar involves directing a beam of microwave radiation at the snowpack and measuring the reflected energy to determine snow cover characteristics. Since this radiation can penetrate into the pack, it can be used to provide information about snowpack stratigraphy and liquid-water content as well as SWE if sufficient information about surface cover and topography is available.

5.3.3.8 Satellite Observation

Satellite imagery using visible, infrared, and microwave wavelengths provides information on the areal extent of snow cover for large areas (Frei et al. 2012). The most accurate maps of areal snow cover to date have been produced from visible-wavelength images, although careful interpretation is required to distinguish snow from clouds and to identify snow in areas of forest and highly reflective land surfaces. Weekly maps have been produced since 1966 for Northern Hemisphere land with a resolution of about 1.2 km^2 (Robinson et al. 1993; http://climate.rutgers.edu/snowcover/). The National Operational Hydrologic Remote Sensing Center (NOHRSC) provides daily maps of snow cover for the United States and the Northern Hemisphere developed from satellite data on its website (http://www.nohrsc.noaa.gov/nh_snowcover). These maps are based on automated analyses of satellite-borne radiometer data using reflected and emitted energy in several visible and infrared wavelengths to differentiate between clouds and snow and to correctly interpret variations produced by forest cover and shading. NOHRSC also assimilates daily ground-based, airborne, and satellite snow observations into a snow model that computes information on snow cover and SWE, snow depth, snowpack temperatures, snowmelt, sublimation, snow-surface energy exchanges, and precipitation at 1-km^2 spatial resolution and hourly temporal resolution.

Parajka et al. (2010a) developed a method for snow-cover mapping using daily MODIS/Terra satellite observations, even with cloud covers as high as 90%. Larson et al. (2009) showed that GPS receivers installed for studies of plate tectonics, geodetic surveying, and weather monitoring can be used to measure snow depth, and possibly density (and therefore SWE) as well. As there are hundreds of such receivers in snowy regions of the United States, these stations may provide a useful supplement for remote observation of snow properties. Two more recent studies (Seo et al. 2010; Su et al. 2010) indicate that observations from the GRACE satellite system, which measures total water-storage change (see section 1.8.2.4), can be used in conjunction with other satellite observations to infer SWE.

5.3.3.9 Overview

In spite of their slight tendency to over measure, snow-survey observations are usually considered the most accurate "routine" measurements of SWE. However, they are labor intensive and impractical for routine use in remote areas. Snow pillows are generally accurate and are widely used in the western United States for remote monitoring of mountain

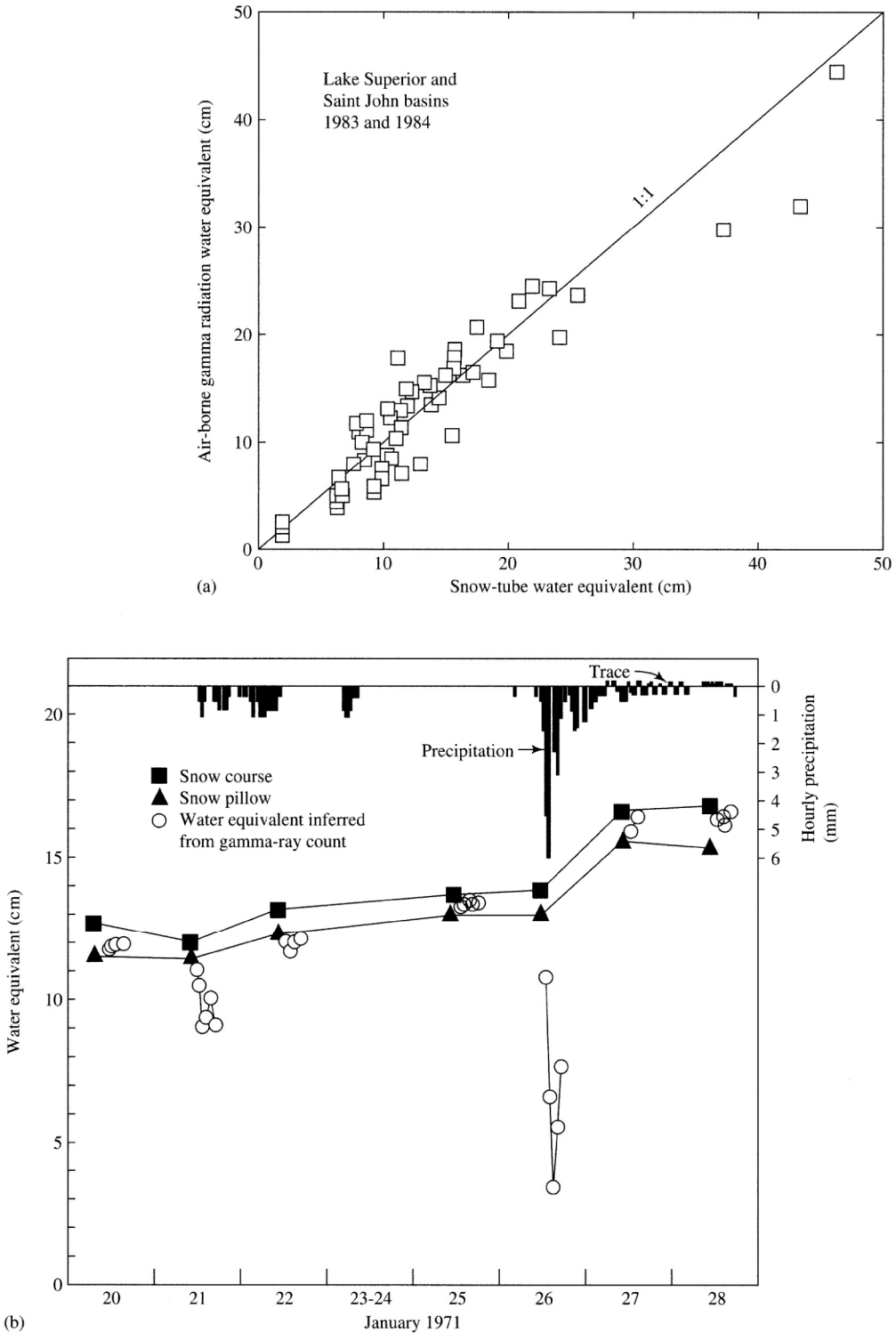

Figure 5.11 (a) Comparison of water equivalent determined by airborne gamma-radiation sensors and snow-tube measurements in the Lake Superior and St. John River basins, United States and Canada [Carroll and Voss (1984)]. (b) Water equivalent of snowpack at Danville, Vermont, measured over 9 days by snow tube, snow pillow, and attenuation of natural gamma radiation. The false low readings of the radiation detector were due to radioactivity deposited during snow storms and could easily be corrected for [Bissell and Peck (1973). Monitoring snow water equivalent by using natural soil radioactivity. *Water Resources Research* 9:885–890, with permission of the American Geophysical Union].

snowpacks (SNOTEL); however, they are subject to bridging, temperature effects, and failures of instrument components (Goodison et al. 1981; McGurk et al. 1993).

Figure 5.11b compares SWE measured via snow tube, snow pillow, and a fixed radio-isotope gauge over several days at one location. Natural radioactivity deposited with falling snow caused false low readings by the gamma detector, but this was found to decay rapidly and could readily be corrected for (Bissell and Peck 1973). Thus all three methods appear to give similar results. Goodison (1981) compared snow-survey and snowfall data in Canada and found that compatible estimates of regional SWE were possible only if: (1) snow-survey data are weighted to account for the variability of SWE as a function of land use and (2) precipitation-gauge measurements of snowfall are corrected for gauge-catch deficiencies due to wind.

Techniques involving spatial interpolation similar to those described for mapping of areal precipitation (section 4.3.2) have been developed and are routinely used for mapping the areal distribution of SWE in the United States (Carroll and Cressie 1996).

Remotely sensed observations via aircraft or satellite using active or passive microwave, infrared, or visible wavelengths are now the main source of information on the areal extent of snow cover. As noted, the NOHRSC program makes these readily available for the United States and the Northern Hemisphere. Such observations, along with water-equivalent information developed from telemetered remote snow pillows and airborne detection of gamma radiation, are widely used for water-resource management decisions, especially in the western United States.

5.3.4 Snowmelt, Ablation, and Water Output

5.3.4.1 Lysimeters

The most straightforward method for measuring water output is via a **lysimeter** (figure 5.10), which collects the water draining from the overlying snow and directs it to a device that records the flow (Haupt 1969). This instrument may be fitted with a circular metal ring that can be electrically heated and lowered through the snow to isolate the cylinder of snow above the collecting surface to avoid gaining or loosing water that might be moving horizontally along ice layers in the snowpack. As with snow pillows, snow conditions above a lysimeter may differ from those in the natural snowpack due to interruption of the snow-ground connection.

5.3.4.2 Snow Pillows

Snow pillows detect ablation as a decrease in weight (assuming the water runs off the pillow); in many cases evaporation can be considered negligible and the weight change can be attributed to water output.

5.3.4.3 Universal Gauge

As noted in section 5.3.1.2, universal gauges collect and measure water output. Water output occurring at the same time as a corresponding weight decrease would indicate snowmelt; water output in the absence of a weight decrease indicates rainfall; and a weight decrease in the absence of water output indicates evaporation.

5.3.4.4 Pans

Specific measurement of snowpack evaporation and sublimation can be made using pans that are periodically weighed. Slaughter (1966) reviewed studies that employed various types of pans, and concluded that good measurements can be obtained using pans made of plastic or metal as long as the edge of the pan is flush with the snow surface and the surface roughness of the snow in the pan is the same as that of the surrounding snowpack. The pan should be at least 10 cm deep to avoid absorption of radiation by the pan bottom and, if significant melt is occurring, should be designed to allow meltwater to drain into a collector for separate measurement.

5.4 Distribution of Snow

Snow accumulation and properties are highly dependent on local topography and site factors such as aspect (slope orientation) and vegetation cover. For example, Rice and Bales (2010) found that snow depths during both accumulation and ablation periods varied by up to 50% due to the variability of topography and vegetation across a small (0.4 ha) study area in the Sierra Nevada of California. In general, local variability will be greatest in regions where periods of melting occur during the winter, where there are pronounced spatial changes in land cover and topography, and where much of the heat input to the snow is from solar radiation. Snow drifting during storms can produce large variations in snow depth and density over short distances, and variations in subsequent snow metamorphism, melt-

ing, and evaporation due to local wind, temperature, radiation, and other microclimatic conditions can further modify the distribution of these properties.

Clark et al. (2011a) reviewed field studies in different snow environments globally. They found that spatial variability of SWE is shaped by several processes that occur across a range of spatial scales. At the watershed scale, spatial variability is shaped by variability in meteorological factors such as elevational gradients in temperature, which can be estimated by spatial interpolation. However, spatial variability of SWE at the hillslope scale is caused by very local processes such as drifting, sloughing of snow from steep slopes, trapping of snow by shrubs, and the unloading of snow by the forest canopy, which are more difficult to resolve explicitly. Based on their analysis, Clark et al. (2011a) provided guidance on approaches to representing these local processes and on the suitability of several common snow-modeling approaches.

Mizukami et al. (2011) developed a simple regional regression-based approach using readily available geographic and meteorological parameters as predictors to map SWE climatology in the mountainous areas of the western United States. The spatial and temporal resolution of the analysis was based on the resolution of available meteorological data, 4 km and 1 month, respectively. The method provided reliable predictions from October to March, but broke down in April because processes at finer space and time scales affected SWE.

Noting that snow-distribution patterns are similar from one year to the next because they are largely controlled by the interaction of topography, vegetation, and consistent synoptic weather patterns, Sturm and Wagner (2010) identified climatological snow distribution patterns for a tundra watershed. Using these empirically based patterns, along with a few depth measurements, they could model the snow-depth distribution as well or better than the output from a weather-driven, physically based snow model. The distribution patterns can be captured via aerial photography or satellite remote sensing.

Thus snow characteristics will be highly variable in space due largely to variations in vegetative cover, slope, and aspect; consequently, obtaining a representative picture of the distribution of snow and snow properties is important, and usually difficult. Remotely sensed information that simply identifies areas with and without snow cover can be extremely valuable in assessing the amount of water present as snow. Peck (1997) emphasized that particular care is needed in obtaining reliable hydrometeorological measurements in cold regions, and stressed that a smaller number of high-quality records may be more valuable than a larger number of records of questionable quality.

5.4.1 Effects of Elevation and Aspect

Because of the general decrease of air temperature with altitude (figure 2.2), the amount and fraction of precipitation falling as snow are usually strong functions of elevation in a region (figure 5.12). Rates of increase of SWE with elevation vary regionally and with local factors such as aspect, and may vary from year to year at a given location. Meiman (1968) reviewed a number of studies on the elevational distribution of snow in North America, and reported rates of increase of SWE ranging from 5.8 to 220 mm per 100 m elevation. Caine (1975) found that the year-to-year variability of SWE decreased with elevation in the southern Rocky Mountains of the United States.

The main effect of aspect is on energy inputs from solar radiation, resulting in faster densification and melting on south-facing slopes. Aspect may also affect the wind microclimate, which in turn affects snow deposition and densification and energy exchanges of sensible and latent heats. These energy exchanges are discussed quantitatively in section 5.5; Donald et al. (1995) developed relations between land-cover types and SWE and other snow properties in Ontario, Canada, that are useful for snowmelt modeling.

5.4.2 Effects of Vegetation

The accumulation of precipitation on the leaves and branches of vegetation is called **canopy interception**. Some intercepted snow eventually falls to the ground either before or after melting and is added to the snowpack; the rest evaporates and is called **canopy interception loss**.[2] Deciduous trees intercept less snow than do conifers, and various conifer species differ in their capture of snow. Schmidt and Gluns (1991) found that (1) individual conifer branches intercepted 11 to 80% of SWE in 22 storms, (2) the fraction intercepted was inversely related to snow density and to total storm precipitation, and (3) the maximum intercepted water equivalent was about 7 mm. Thus, although forests intercept a large proportion of snowfall, most studies have found that this is of minor hydrologic impor-

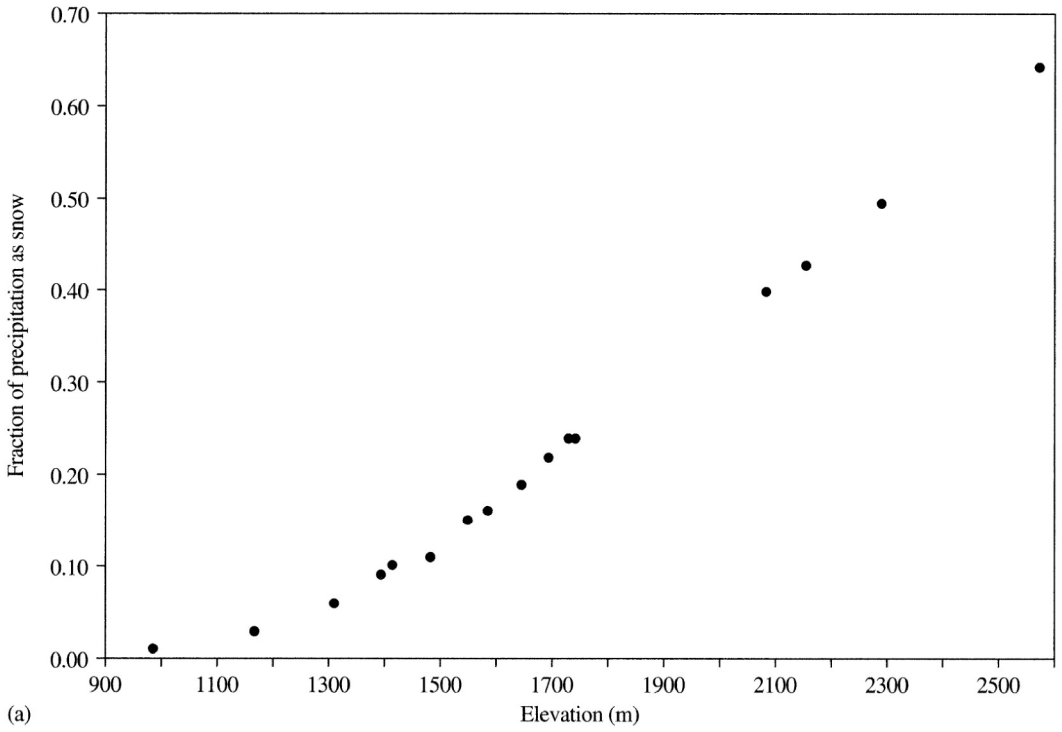

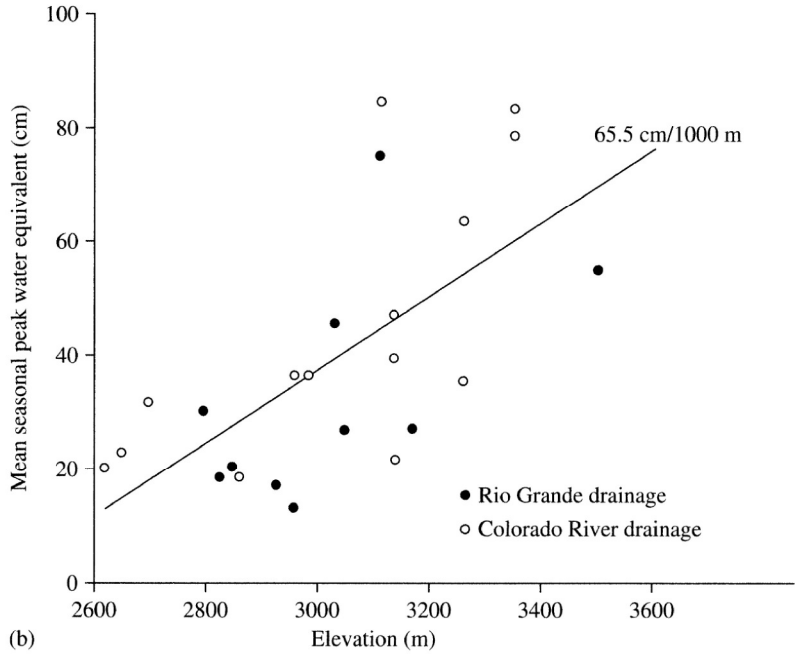

Figure 5.12 (a) Fraction of precipitation occurring as snow as a function of elevation in the San Bernardino Mountains of southern California [data from Minnich (1986)]. (b) Annual peak water equivalent as a function of elevation, San Juan Mountains, Colorado [Caine (1975). An elevational control of peak snowpack variability. *Water Resources Research* 11:613–621, courtesy of American Water Resources Association].

tance because most intercepted snow falls to the ground in solid or liquid form rather than evaporates (Hoover 1971; Tennyson et al. 1974).

In a study in New Mexico, Veatch et al. (2009) found that SWE is significantly correlated with canopy density and that maximum snow accumulation occurred in forests with canopy densities between 25 and 40%. Forest edges affected snow depth, with clearings shaded by forest to their immediate south having ~25% deeper snow than either large open areas or densely forested areas.

Forest clearings disrupt the typical upward-increasing wind velocities above a canopy (section 3.5.2) and affect snow deposition. Accumulation tends to be greater in small clearings (i.e., those with diameters less than 20 times the height of surrounding trees) than in the surrounding forest, but the pattern is typically reversed in larger clearings because wind speed tends to be higher, blowing snow into the surrounding forest and causing higher evaporation in the clearing (Golding and Swanson 1986). Watershed-scale experiments have shown that tree harvesting tends to increase SWE and snowmelt runoff (Schmidt and Troendle 1989). This increase is attributed to a reduction in the evaporation of intercepted snow and increased snow deposition into clearings and thinned forests, which is only partially offset by increased evaporation from the ground snowpack.

Figure 5.13 on the following page shows the variability of seasonal peak depth, density, and SWE on a range of vegetation types in Ontario, Canada. Overall these observations are consistent with those just described for forest clearings: the highest depths and water equivalents were in an open forest with shrub understory (vegetation zone B), and the lowest values were in areas without forest cover, including grass (vegetation zone A) and marsh (Adams 1976). Density tended to vary little with land-cover type. Note also that there was considerable year-to-year variability in the relative values.

Varhola et al. (2010) reviewed studies of the overall effects of forest cover on snow accumulation and melt rates at 65 locations, mostly in the United States and Canada. They were able to summarize the results in two simple empirical relations between fractional changes in forest cover, ΔF, and fractional changes in seasonal accumulation, ΔAcc, and melt rates, ΔM:

$$\Delta Acc = -0.40 \cdot \Delta F, \quad \textbf{(5.13)}$$

$$\Delta M = -0.53 \cdot \Delta F. \quad \textbf{(5.14)}$$

The negative relation in accumulation is attributed to increased sublimation of snow intercepted in the forest canopy; the negative relation in melt rates is largely due to the effects of shading in reducing energy flux from solar radiation. They noted that there was considerable scatter around these relations due to local conditions.

On a very local scale, Woo and Steer (1986) presented data on variations of snow depth around individual trees in a subarctic spruce forest in northern Ontario. The data were used along with information on tree spacing to compute average snow depth for the forest. As shown in figure 5.14, depth increases away from the trunk and reaches the clearing value at a distance of 2 to 4 m from the tree. Presumably, this pattern is produced by snow interception and by added heat inputs due to longwave radiation from the tree trunk, which can accelerate the processes that increase snow density and produce melt.

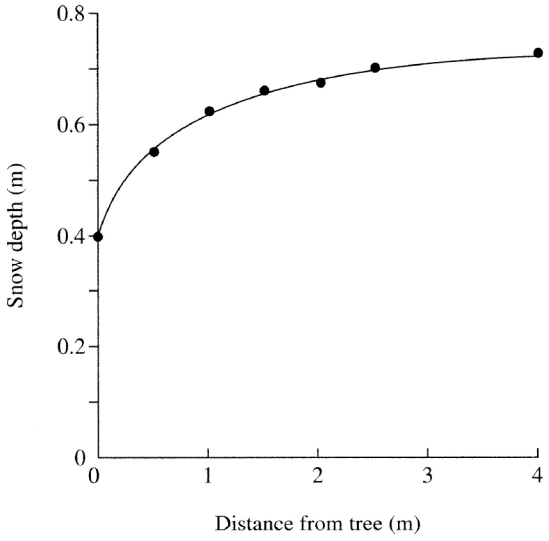

Figure 5.14 Snow depth as a function of distance from a tree in a spruce forest in northern Ontario [data of Woo and Steer (1986)].

5.5 Snowmelt Processes

Much of our understanding of snowmelt processes and the forecasting of snowmelt runoff originated with an intensive, several-year research program conducted by the US Army Corps of Engineers at the Central Sierra Snow Laboratory (Cali-

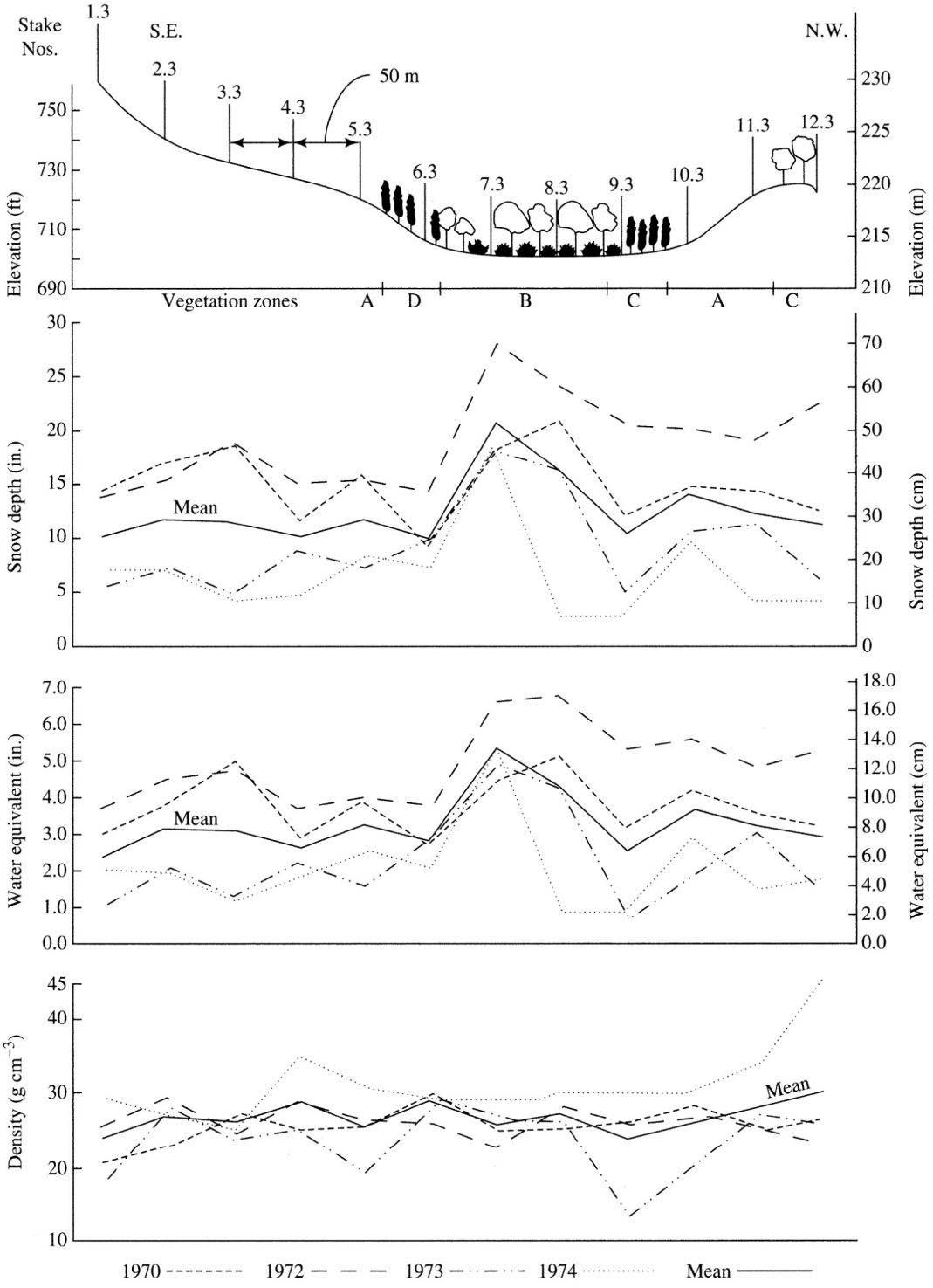

Figure 5.13 Peak seasonal snow properties along a transect near Peterborough, Ontario, for four winters. Vegetation zones: A = grass; B = open deciduous forest with shrub understory; C = moderately dense deciduous and coniferous forest; D = dense cedar forest [Adams (1976). Areal differentiation of snow cover in east central Ontario. *Water Resources Research* 12:1226–1234. with permission of the American Geophysical Union].

fornia) in the early 1950s; the results of this research are summarized in the iconic US Army Corps of Engineers (1956) report entitled *Snow Hydrology*. That and subsequent work on snowmelt dynamics sponsored by the NWS (Anderson 1973, 1976), and on the flow of water through snow by the US Army Cold Regions Research and Engineering Laboratory (Colbeck 1971, 1978), form the basis of our current understanding of snowmelt processes.

5.5.1 The Snowpack Energy Balance

The energy balance for the snowpack element of figure 5.5 is

$$Q_{melt} + \frac{\Delta U}{\Delta t} = F_E, \qquad \textbf{(5.15)}$$

where Q_{melt} [E L^{-2} T^{-1}] is the rate at which energy becomes available for snowmelt, F_E is the net flux of energy [E L^{-2} T^{-1}] from the atmosphere and ground, and $\Delta U/\Delta t$ is the change in internal energy (temperature) in time period Δt. The components of the energy flux are

$$F_E = K + L + \lambda E + H + R + G, \qquad \textbf{(5.16)}$$

where K is net shortwave (solar) radiation flux, L is net longwave radiation flux, λE is net flux of latent heat from the atmosphere via turbulent diffusion, H is net flux of sensible heat from the atmosphere via turbulent diffusion, R is flux of sensible heat from rain, and G is the net flux of sensible heat via conduction with the ground.

A seasonal snowpack begins to form when average air temperatures are more or less continually below 0°C. As the snowpack accumulates, net inputs of energy from the atmosphere are generally negative, average snowpack temperature decreases, and water equivalent typically increases. The period of general increase of snowpack water equivalent prior to the melt period is called the **accumulation period**. The **melt period** of a seasonal snowpack begins when the net input of energy becomes more or less continually positive. The melt period can usually be separated into three phases:[3]

1. **Warming phase**, during which the average snowpack temperature increases more or less steadily until the snowpack is isothermal at 0°C.
2. **Ripening phase**, during which melting occurs but the meltwater is retained in the snowpack. At the end of this phase the snowpack is **ripe**, i.e., it is isothermal and cannot retain any more liquid water.
3. **Output phase**, during which further inputs of energy cause melting that leaves the snowpack as water output.

In most situations, the snowpack does not progress steadily through this sequence: Some melting usually occurs at the surface of a snowpack from time to time prior to the ripening phase, when air temperature rises above 0°C for periods of hours or days. The meltwater thus produced percolates into the cold snow at depth and refreezes, releasing latent heat, which raises the snow temperature. Similarly, snow-surface temperatures may fall below freezing during the melt period, and the surface layer must warm again before melting can continue. Even where daytime temperatures are continuously above freezing, temperatures commonly fall below 0°C at night and it may take several hours for the snowpack to warm and resume melting each day (Bengtsson 1982; Tseng et al. 1994). Nevertheless, the above phases provide a useful context for understanding the melt process. Examples of calculations of the net energy inputs required for completion of each of the melt phases are given in box 5.2.

5.5.1.1 Warming Phase

During the warming phase there is no melt, and net energy inputs warm the snowpack, so from (5.15) and (5.16),

$$\frac{\Delta U}{\Delta t} = F_E = K + L + \lambda E + H + R + G. \qquad \textbf{(5.17)}$$

At any point prior to the warming phase, the **internal energy**, or **cold content**, of a snowpack, U_{cc} [E/L^2], is the amount of energy per unit area required to raise its average temperature to the melting point. Considering again the snowpack of figure 5.5, noting that a cold snowpack contains no liquid water, and neglecting the heat capacity of the air within it,

$$U_{cc} = -c_i \cdot \rho_i \cdot (V_i/A) \cdot (T_s - T_{mp}), \qquad \textbf{(5.18a)}$$

where c_i is the heat capacity of ice (2,102 J/kg · K), T_s is the average temperature of the snowpack (≤ 0°C), T_{mp} is the melting-point temperature (0°C), and the other symbols are as previously defined. Making use of equations (5.1) and (5.7), (5.18a) becomes

$$U_{cc} = -h_s \cdot c_i \cdot \rho_i \cdot (1-\phi) \cdot \left(T_s - T_{mp}\right), \qquad \textbf{(5.18b)}$$

which with (5.5) can be written as

$$U_{cc} = -h_s \cdot c_i \cdot \rho_s \cdot (T_s - T_{mp}), \qquad \textbf{(5.18c)}$$

or with (5.10) as

$$U_{cc} = -c_i \cdot \rho_w \cdot h_{swe} \cdot (T_s - T_{mp}). \qquad \textbf{(5.18d)}$$

Box 5.2 Example Calculations of Energy Involved in Melt Phases

Warming Phase

Consider a snowpack with $h_s = 72.5$ cm, $\rho_s = 400$ kg/m^3, $h_{swe} = 29$ cm, and $T_s = -9$°C. Its cold content is given by equation (5.18c):

$$U_{cc} = -(2{,}102 \cdot \text{J/kg} \cdot \text{K}) \times (1{,}000 \text{ kg/m}^3) \times (0.29 \text{ m}) \times (-9°\text{C} - 0°\text{C}) = 5.49 \text{ MJ/m}^2.$$

If the net energy flux is $F_E = 10.8$ MJ/m^2 · day, the snowpack temperature increase in one day is given by equation (5.20) as

$$\Delta T_s = \frac{(1 \text{ day}) \cdot \left(10.8 \times 10^6 \text{ J/m}^2 \cdot \text{day}\right)}{(2{,}102 \text{ J/kg} \cdot °\text{C}) \cdot \left(1{,}000 \text{ kg/m}^3\right) \cdot (0.29 \text{ m})} = 2.95 \text{ °C}.$$

At this rate it would take

$$\frac{5.49 \text{ MJ/m}^2}{10.8 \text{ MJ/m}^2 \cdot \text{ day}} = \frac{9 \text{ °C}}{17.7 \text{ °C/day}} = 0.508 \text{ days}$$

to complete the warming phase.

Ripening Phase

When the net energy inputs from the atmosphere and ground equal U_{cc} and the snowpack has become isothermal at the melting point, melting and the ripening phase begin. Assuming snowpack density remains at 400 kg/m^3, its liquid-water-holding capacity is estimated via equation (5.25) as

$$\theta_{ret} = 3 \times 10^{-10} \cdot (400 \text{ kg/m}^3)^{3.23} = 0.077.$$

Then from equation (5.23),

$$h_{wret} = 0.077 \cdot (0.725 \text{ m}) = 0.055 \text{ m} = 55 \text{ mm}.$$

The energy required to produce melt that fills this capacity and brings the snowpack to a ripe condition is then found from equation (5.26) with $\lambda_f = 0.334$ MJ/kg:

$$U_r = (0.055 \text{ m}) \times (1{,}000 \text{ kg/m}^3) \times (0.334 \text{ MJ/kg}) = 18.4 \text{ MJ/m}^2.$$

Again assuming $F_E = 10.8$ MJ/m^2 · day, we can calculate the amount of melt water produced in 1 day via equation (5.22):

$$\Delta h_w = \frac{(1 \text{ day}) \cdot \left(10.8 \text{ MJ/m}^2 \cdot \text{day}\right)}{\left(1{,}000 \text{ kg/m}^3\right) \cdot (0.334 \text{ MJ/kg})} = 0.0323 \text{ m} = 32.3 \text{ mm}.$$

At this rate the ripening phase would take

$$\frac{55 \text{ mm}}{32.3 \text{ mm/day}} = 1.70 \text{ days}.$$

Output Phase

The net energy input required to complete the melting of the snowpack is found from equation (5.27):

$$U_o = [(0.29 - 0.055) \text{ m}] \cdot (1{,}000 \text{ kg/m}^3) \cdot (0.334 \text{ MJ/kg}) = 78 \text{ MJ/m}^2.$$

If the energy flux remained constant at $F_E = 10.8$ MJ/m^2 · day, it would take

$$\frac{78 \text{ MJ/m}^2}{10.8 \text{ MJ/m}^2 \cdot \text{day}} = 7.22 \text{ days}$$

to completely melt the snowpack.

The cold content can be computed at any time prior to the ripening phase, and the net energy input required to complete the warming phase equals the cold content at that time.

During the warming phase an increment of energy input ΔU corresponds to an increase in average temperature of the snowpack, ΔT_s, so from equation (5.18d),

$$\Delta U = c_i \cdot \rho_w \cdot h_{swe} \cdot \Delta T_s. \quad \textbf{(5.19)}$$

Substitution of equation (5.17) into (5.19) relates the temperature change in a time interval Δt to the net energy flux:

$$\Delta T_s = \frac{\Delta t \cdot F_E}{c_i \cdot \rho_w \cdot h_{swe}}. \quad \textbf{(5.20)}$$

5.5.1.2 Ripening Phase

The ripening phase begins when the snowpack becomes isothermal at 0°C. At this point, there is no further temperature change and further net inputs of energy produce meltwater that is initially retained in the pore spaces by surface-tension forces (figure 5.15). During this phase equations (5.15) and (5.16) become

$$Q_{melt} = F_E = K + L + \lambda E + H + R + G. \quad \textbf{(5.21)}$$

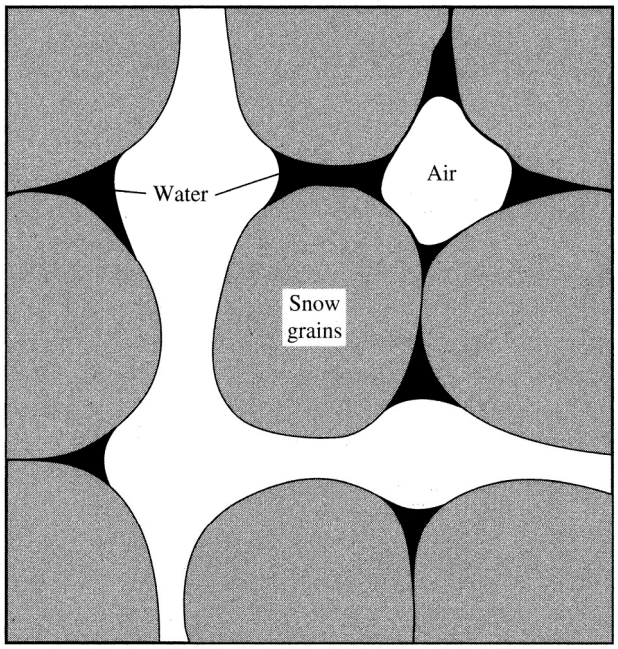

Figure 5.15 An idealized thin section of snow showing snow grains, water retained by surface tension, and continuous pores filled with air [adapted from Colbeck (1971)].

The increase in liquid-water content produced by a given energy flux in a time increment Δt is

$$\Delta h_w = \frac{\Delta t \cdot F_E}{\rho_w \cdot \lambda_f}, \quad \textbf{(5.22)}$$

where λ_f is the latent heat of freezing. The maximum amount of meltwater that can be retained is the **liquid-water-holding capacity**, h_{wret}, which is given by

$$h_{wret} = \theta_{ret} \cdot h_s, \quad \textbf{(5.23)}$$

where θ_{ret} is the maximum volumetric water content that the snow can retain against gravity.[4] Experiments show that θ_{ret} increases with snow density and decreases with grain size, i.e.,

$$\theta_{ret} = f(\rho_s / d) \quad \textbf{(5.24)}$$

(Yamaguchi et al. 2012). However, Goto et al. (2012) found the following empirical relation between θ_{ret} and density for ripe snow, when grain size tends to vary little:

$$\theta_{ret} = 3\times10^{-10} \cdot \rho_s^{3.23}, \quad \textbf{(5.25)}$$

where ρ_s is in kg/m^3 (figure 5.16).

We can use equation (5.25) with previously derived expressions to compute the proportion of pore spaces that are filled with water when $\theta = \theta_{ret}$. For example, for a ripe snowpack with ρ_s = 400 kg/m^3, equation (5.25) gives θ_{ret} = 0.077. Substituting these quantities into equation (5.5) allows us to compute the corresponding porosity, ϕ = 0.647. The ratio θ_{ret}/ϕ is the proportion of pore spaces filled with water at the end of the ripening phase [see equations (5.2) and (5.4)], which for this case is 0.077/0.647 = 0.119. Thus less than 12% of the pore spaces in a typical ripe snowpack contain water, and such snowpacks are far from being saturated.

The net energy input required to complete the ripening phase, U_r, can be computed as

$$U_r = h_{wret} \cdot \rho_w \cdot \lambda_f = \theta_{ret} \cdot h_s \cdot \rho_w \cdot \lambda_f. \quad \textbf{(5.26)}$$

5.5.1.3 Output Phase

Once the snowpack is ripe, further net energy inputs produce meltwater that cannot be held by surface-tension forces against the pull of gravity, and water begins to percolate downward, ultimately to become water output. This flow is more fully described in section 5.6.

The net energy input required to complete the output phase, U_o, is the amount of energy needed to melt the snow remaining at the end of the ripening phase:

$$U_o = (h_{swe} - h_{wret}) \cdot \rho_w \cdot \lambda_f. \quad \textbf{(5.27)}$$

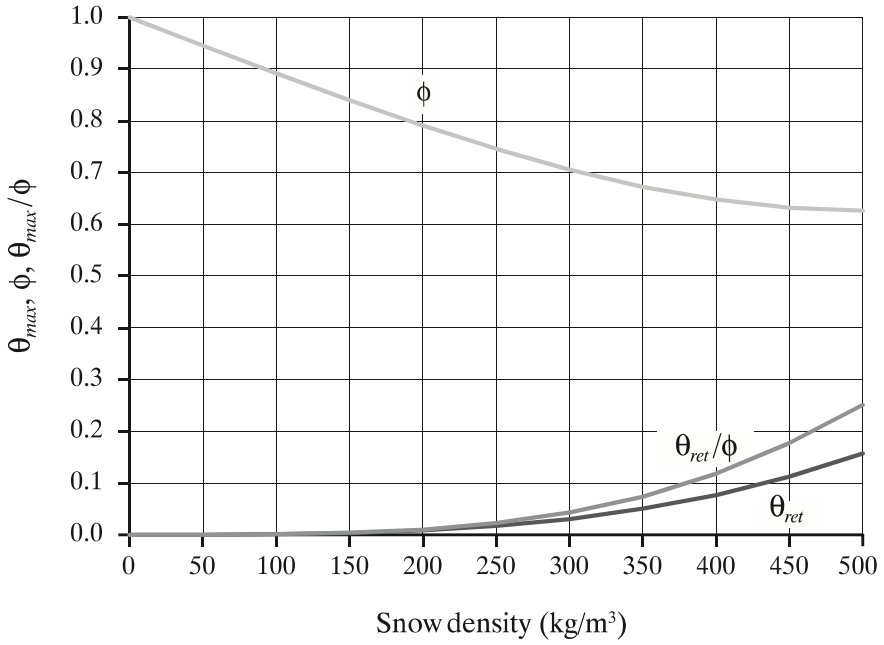

Figure 5.16 Snow porosity, ϕ, maximum water-holding capacity, θ_{ret}, and θ_{ret}/ϕ as a function of snow density, ρ_s. The θ_{ret}/ρ_s relation was measured by Goto et al. (2012) [equation (5.25)]; the other relations were calculated via equation (5.5).

During the output phase, an increase of net energy input, ΔQ_{melt}, is related to a decrease in SWE, $-\Delta h_{swe}$, and an increment of meltwater output, Δw, as

$$\Delta Q_{melt} = -\rho_w \cdot \lambda_f \cdot \Delta h_{swe} \qquad \textbf{(5.28)}$$

and

$$\Delta w = -\Delta h_{swe}; \qquad \textbf{(5.29)}$$

so that

$$\Delta w = \frac{\Delta Q_{melt}}{\rho_w \cdot \lambda_f}. \qquad \textbf{(5.30)}$$

The rate of meltwater production is given by equation (5.22).

5.5.2 Energy-Exchange Processes

The following sections review the basic physics of each of the energy-flux processes of equation (5.16) and introduce approaches to determining their magnitudes. All these energy fluxes vary continuously; the treatment here focuses on *daily* totals or averages, which is a common time-step in hydrologic modeling.

5.5.2.1 Shortwave (Solar) Radiation

The sun's energy is electromagnetic radiation with wavelengths less than 4 μm; most of this energy is concentrated in the visible range between 0.4 and 0.7 μm (figure 2.4). K is the net flux of solar energy entering the snowpack, so

$$K \equiv K_{in} - K_{out} = K_{in} \cdot (1 - a), \qquad \textbf{(5.31)}$$

where K_{in} is the flux of solar energy incident on the snowpack surface (**insolation**), K_{out} is the reflected flux, and a is the shortwave reflectance, or **albedo** [equation (2.7), table 2.4]. Continuous measurements of K values representative of local areas can be obtained with **pyranometers** [described in Iqbal (1983)], facing upward to measure K_{in} and downward to measure K_{out}. However, pyranometers are installed at only a few permanent locations (see figure D.1) and research stations. Hourly, daily, and monthly insolation values representative of large areas (~0.5° latitude × 0.5° longitude) can be obtained from Geostationary Operational Environmental Satellite (GOES) observations (Justus et al. 1986), but the data are subject to error over areas with significant snow cover (Lindsey and Farnsworth 1997).

Because of the difficulty in obtaining reliable insolation measurements at appropriate space and time scales, other approaches are usually needed to provide values of K or K_{in}. These approaches begin with values of the flux of solar radiation arriving at the outer edge of the earth's atmosphere, the **extraterrestrial solar radiation** which, as described in appendix D, is an astronomically determined function of (1) latitude; (2) declination angle of the sun, which varies sinusoidally through the year (figure 5.17); and (3) the zenith angle of the sun, which varies with time of day. Total daily extraterrestrial radiation is computed by integrating the instantaneous values between the times of sunrise and sunset, which are functions of latitude and declination.

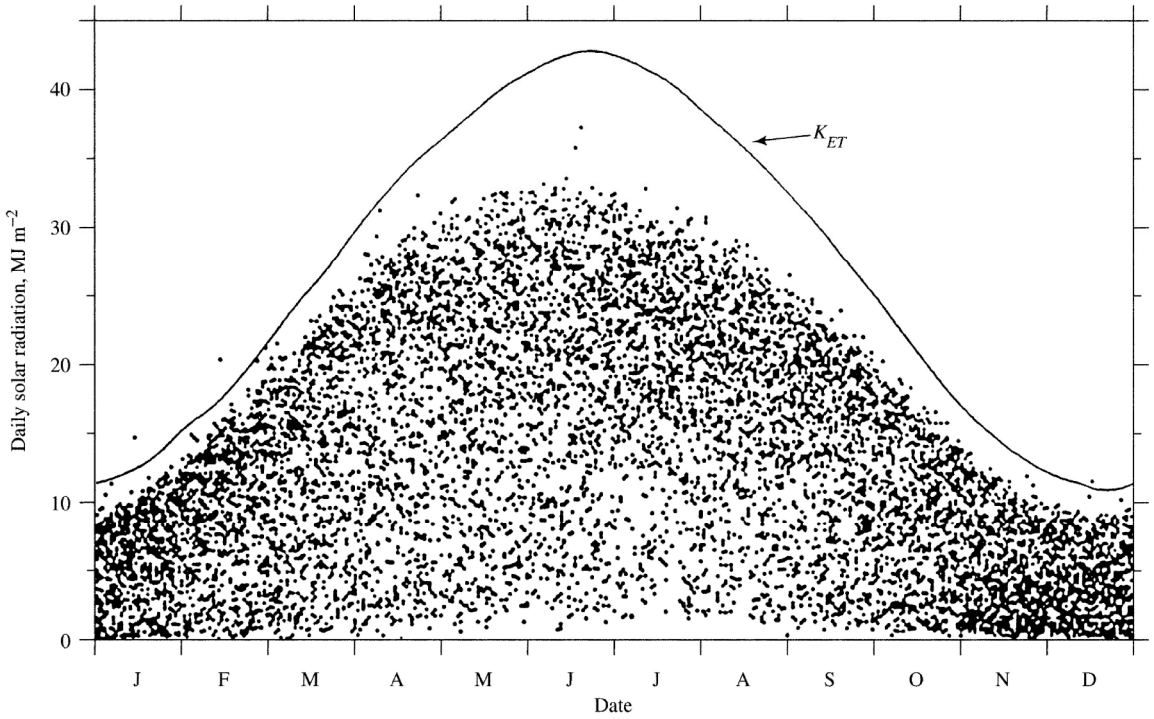

Figure 5.17 Extraterrestrial, K_{ET}, and incident, K_{in}, solar radiation on a horizontal surface, at West Thornton, New Hampshire, for 1960 through 1987. Each dot represents measured K_{in} for a day [Federer et al. (1990)].

5.5.2.1.1 Clear-Sky Shortwave Radiation

Figure 5.18 illustrates the factors affecting the flux of solar radiation incident at the surface. As it passes through the atmosphere, the energy in the solar beam is diminished by absorption and reflectance (scattering) by atmospheric gases and aerosols, reflection by clouds, and shading by vegetation. In the absence of clouds, vegetation, and any topographic shading (which can be important in mountainous areas), the *clear-sky* solar flux on a horizontal surface, K_{CSh}, includes both the energy in the direct solar beam, K_{dir}, diffuse radiation, K_{dif}, and backscattered radiation, K_{BS}:

$$K_{CSh} = K_{dir} + K_{dif} + K_{BS}. \qquad \textbf{(5.32)}$$

As developed in appendix D, the terms on the right-hand side of (5.32) can be expressed as fractions of extraterrestrial radiation, so we can write

$$K_{CSh} = \tau_{atm} \cdot K_{ET}, \qquad \textbf{(5.33)}$$

where τ_{atm} represents the total atmospheric effect on extraterrestrial radiation ($0 < \tau_{atm} < 1$). The effects of clouds and vegetation can be similarly represented as

$$K_{inh} = \tau_C \cdot \tau_F \cdot K_{CSh} = \tau_C \cdot \tau_F \cdot \tau_{atm} \cdot K_{ET} \qquad \textbf{(5.34)}$$

where K_{inh} is the insolation on a horizontal surface, $(1 - \tau_C)$ and $(1 - \tau_F)$ are the effects of shading by clouds and forest, respectively, and $0 \le \tau_C, \tau_F \le 1$.

5.5.2.1.2 Effect of Cloud Cover

The effect of clouds on insolation can be estimated using several empirical approaches:

- **Estimation based on sky cover**: The fraction of sky covered by clouds, C, was formerly recorded manually by weather observers at about 250 weather stations in the United States. These observations can be used to estimate the effect of cloud cover using empirical relations such as

$$\tau_C = 0.355 + 0.68 \cdot (1 - C) \qquad \textbf{(5.35)}$$

(Croley 1989). In snow studies, the US Army Corps of Engineers (1956) used a relation involving cloud height:

$$\tau_C = 1 - (0.82 - 7.9\times10^{-5} \cdot Z_C) \cdot C, \qquad \textbf{(5.36)}$$

where Z_C is cloud-base height in meters. However, manual observations of C are no longer being made in the United States because human weather observers are being replaced by automated stations (ASOS; box 4.4).

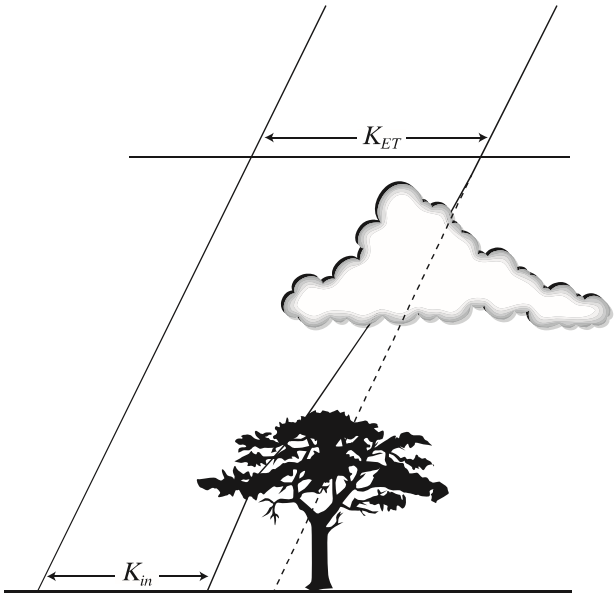

Figure 5.18 Schematic diagram of factors affecting the flux of solar radiation incident at the surface. As it passes through the atmosphere, the energy in the solar beam is diminished by absorption and reflectance (scattering) by atmospheric gases and aerosols, reflection and absorption by clouds, and shading by vegetation.

- **Estimation based on "percent possible sunshine"**: Where available, daily observations of the fraction of daylight hours receiving bright sunshine, $\mathcal{S}$, have been used to estimate insolation via nomographs (Hamon et al. 1954), or empirical formulas such as

$$\tau_C = k_1 + k_2 \cdot \mathcal{S}, \qquad \textbf{(5.37)}$$

where $0.18 \le k_1 \le 0.40$ and $0.42 \le k_2 \le 0.56$ (Gray and Prowse 1992); Shuttleworth (1992) recommended using $k_1 = 0.25$ and $k_2 = 0.50$. Daily observations of $\mathcal{S}$ have been made at some US weather stations, but the availability of these is decreasing as stations become automated (Lindsey and Farnsworth 1997).

- **Estimation based on maximum and minimum temperature and precipitation**: Daily temperature range tends to be inversely related to cloud cover, and there have been several attempts to use this relation to develop empirical relations between insolation and daily temperature range. Hunt et al. (1998) proposed a relation based on measurements in Canada:

$$K_{inh} = k_0 \cdot (T_M - T_m)^{1/2} \cdot K_{ET} + k_1 \cdot T_M + k_2 \cdot P + k_3 \cdot P^2 + k_4, \qquad \textbf{(5.38)}$$

where T_M is daily maximum temperature (°C), T_m is daily minimum temperature (°C), P is daily precipitation (mm), and k_0–k_4 are empirical constants. Unfortunately, the values of the coefficients in (5.38) were not given; however, the form of the model may be applicable generally. Hunt et al. (1998) found that if the location at which estimates are required is less than 400 km from a station where there are pyranometer measurements, the measured values should be used; otherwise equation (5.38) using local meteorological data gave better estimates.

5.5.2.1.3 Effect of Forest Canopy

The effect of forest canopy on insolation is related to (1) the ratio of the horizontally projected area of forest canopy to the total area of interest, F, which can be determined from air photographs, satellite images, or ground-based hemispherical photography; and (2) the thickness and type of canopy. These relations are complicated by multiple reflections and differing effects of the canopy on direct and diffuse radiation (Hardy et al. 2004; Mahat and Tarboton 2012). A commonly used quantity that reflects both canopy extent and thickness is the **leaf-area index** (***LAI***), which is the ratio of total leaf area to ground-surface area; typical values of *LAI* for common forest types are tabulated in table 6.4.

Figure 5.19 shows values of τ_F for four types of conifer forest and leafless deciduous forest as a function of forest cover only; the relationship for lodgepole pine can be approximated as

$$\tau_F = \exp(-3.91 \cdot F). \qquad \textbf{(5.39)}$$

Mahat and Tarboton (2012) measured seasonal average values of $\tau_F = 0.36$ for conifer forest and $\tau_F = 0.79$ for deciduous forest. Wang et al. (2010) suggested a general model for τ_F as a function of leaf-area index:

$$\tau_F = (1 - a_F) \cdot (1 - a_s) \cdot \exp(-LAI), \qquad \textbf{(5.40)}$$

where a_F is the albedo of the vegetation (assumed = 0.13) and a_s is the albedo of snow under the canopy (assumed = 0.5). Because the effect of vegetative cover in reducing incident shortwave radiation depends on the type, height, and spacing of the plants, these relations must be applied with caution for other situations.

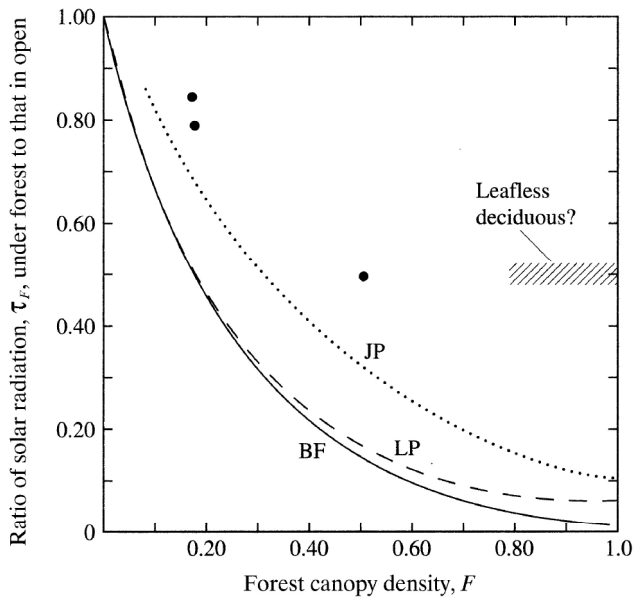

Figure 5.19 Ratio of incident solar radiation, τ_F, under various types of forest canopies to that received in the open for four forest types. BF = balsam fir, JP = jack pine, LP = lodgepole pine, circles = open boreal spruce forest [Dunne and Leopold (1978)].

5.5.2.1.4 Effect of Slope and Aspect

As shown in appendix D, incident solar-radiation flux on a slope is a function of the slope azimuth angle (**aspect**, α) and angle of inclination (slope, β) relative to the solar beam. This effect can be calculated by noting that a sloping surface at a given location is parallel to a horizontal surface at another location, and receives the same flux of direct clear-sky solar radiation as that horizontal surface. The **equivalent latitude** (figure 5.20) and **equivalent longitude** of this slope can be calculated as functions of latitude, day-of-year (the number of days since the calendar year began, sometimes called the "Julian date"), slope azimuth angle, and slope inclination angle [equations (D.24) and (D.25)]. Figure 5.21 shows the very large differences in insolation on north- and south-facing slopes at a midlatitude location during the snowmelt season.

5.5.2.1.5 Albedo

The physics of reflection are complicated (see, for example, Melloh et al. 2002; Yasunari et al. 2011); snow-surface albedo depends on wavelength, snow depth, grain size and shape, liquid-water content, sun angle, and impurities (Gardner and Sharp 2010). Its value ranges from about 0.2 to 0.9, and is thus an important determinant of the net input of energy to the snowpack. Albedo generally decreases with the age of the snow surface (time since last snowfall) as density, grain size, and liquid-water content increase and impurities accumulate (figure 5.22b).

Because of the porous nature of snow, solar radiation is reflected not at the surface plane, but over a finite depth. There is little penetration of solar radiation below about 10 cm, so figure 5.22a applies only when $h_s > 10$ cm. For shallower snowpacks, significant amounts of radiation are absorbed by the ground and may heat the snow from below. Leonard and Eschner (1968) found that albedo measured for snow intercepted on a conifer forest was considerably lower ($a \approx 0.2$) than for a ground snowpack, resulting in more rapid melting and greater evaporation for intercepted snow.

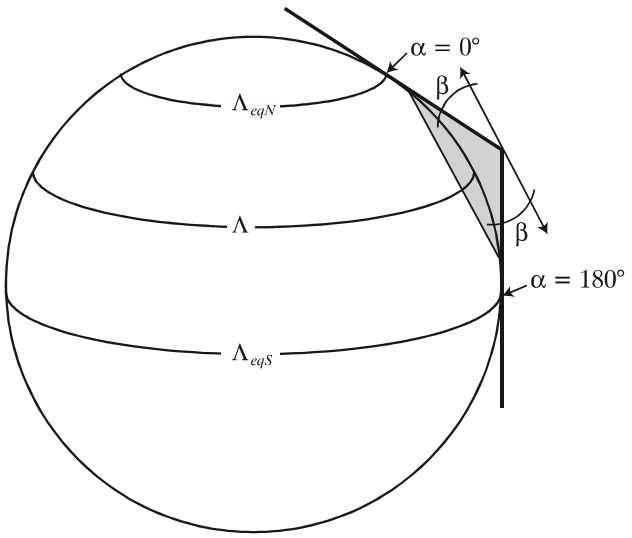

Figure 5.20 Diagram illustrating the equivalent-latitude concept. The shaded triangle represents north- (α = 0°) and south- (α = 180°) facing hillslopes at latitude Λ. The north-facing hillslope is parallel to a horizontal surface at Λ_{eqN}, the south-facing hillslope is parallel to a horizontal surface at Λ_{eqS}. Λ_{eqN} and Λ_{eqS} are the respective equivalent latitudes that are a function of Λ, the slope direction, α, and the slope inclination, β (section D.3).

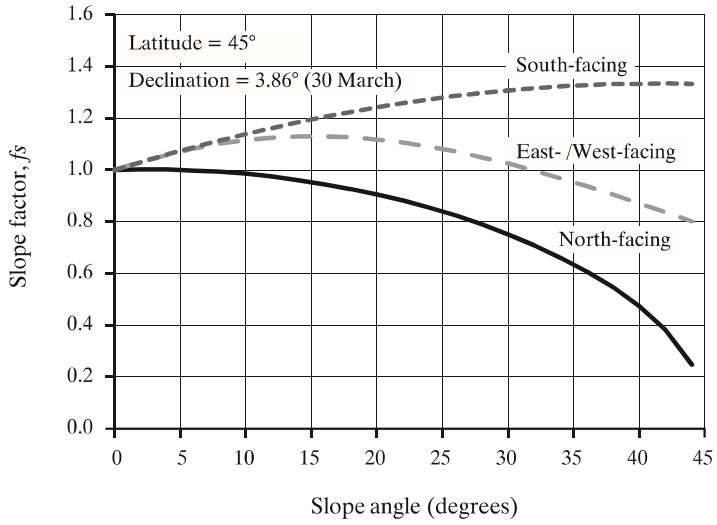

Figure 5.21 Slope factor (≡ ratio of incident solar radiation on slope to that on a horizontal surface) for north-, east- or west-, and south-facing slopes at latitude 45°N on 30 March.

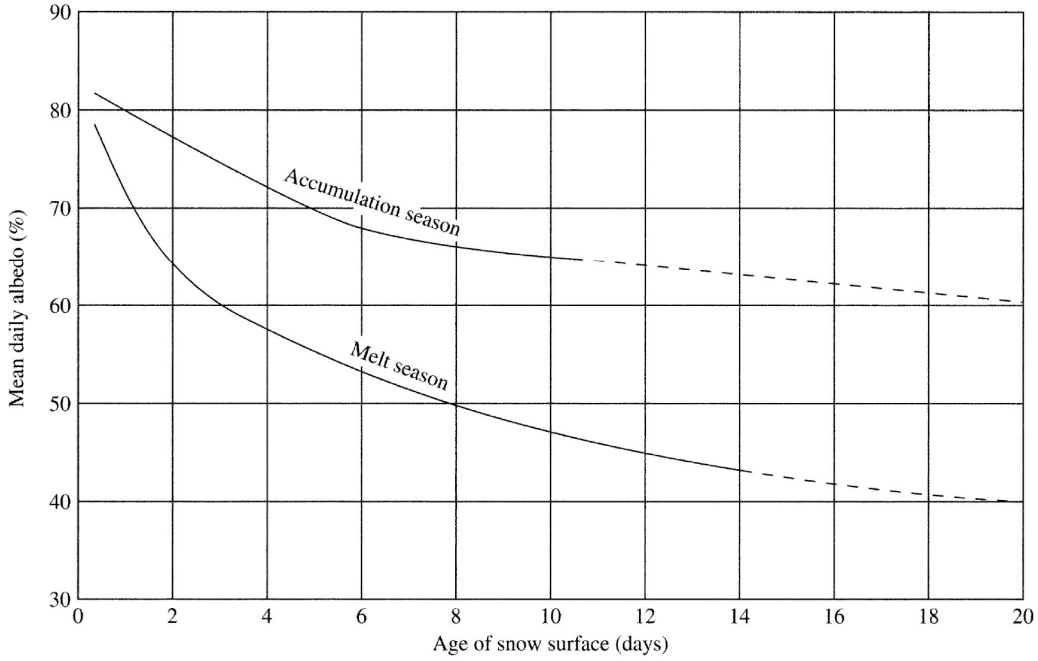

(a)

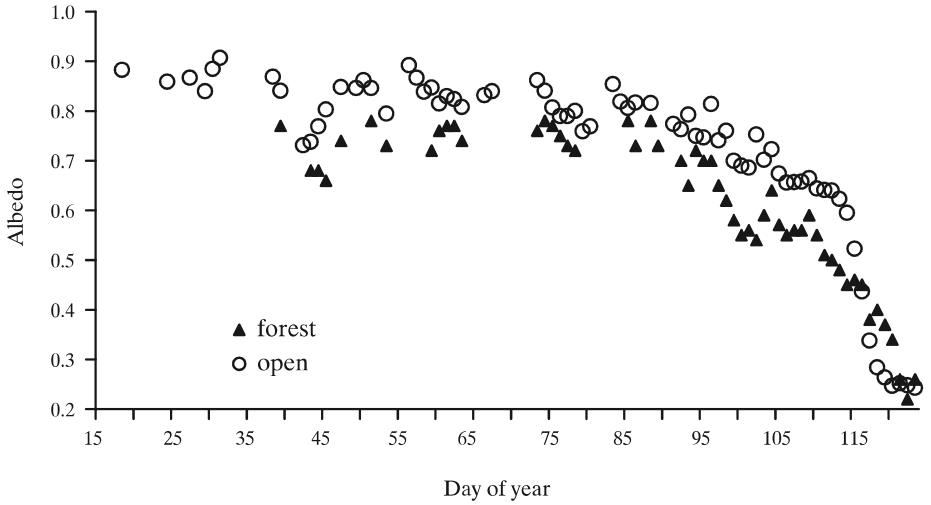

(b)

Figure 5.22 (a) General relation between albedo and age of snow surface (i.e., time since last snowfall) [US Army Corps of Engineers (1956)]. (b) Albedo at forest and open sites at Danville, Vermont, during the snow season of 2001 [Melloh et al. (2002)].

5.5.2.2 Longwave Radiation Exchange

Longwave (also called terrestrial, thermal, or infrared) radiation is electromagnetic radiation with wavelengths of 4 to 60 μm emitted by materials at near-earth-surface temperatures (section 2.1.3.2; figures 2.3 and 2.4). The net input of longwave energy, L, is the difference between the incident flux, L_{in}, emitted by the atmosphere, clouds, and overlying forest canopy and the outgoing radiation from the snowpack, L_{out}:

$$L \equiv L_{in} - L_{out}. \qquad \textbf{(5.41)}$$

Longwave radiation can be measured directly by means of **pyrgeometers** or as the difference between all-wave radiation measured by a **radiometer** and shortwave radiation measured by a pyranometer. However, such instruments are seldom installed except at sites of intensive research, and routine measurements of longwave radiation are available at only a few locations. Thus, as with shortwave radiation, the longwave component of the energy balance is usually estimated from more readily available meteorological information; this estimation is based on the following considerations.

The flux of electromagnetic radiation emitted by a surface is given by the Stefan–Boltzmann equation [equation (2.1)]. Hence we can write

$$L_{in} = \varepsilon_{at} \cdot \sigma \cdot \mathcal{T}_{at}^{\,4}, \qquad \textbf{(5.42)}$$

where ε_{at} is the integrated effective emissivity of the atmosphere and forest canopy, σ is the Stefan–Boltzmann constant ($\sigma = 4.90\times10^{-9} \cdot \text{MJ/m}^2 \cdot \text{K}^4 \cdot \text{d}$), and $\mathcal{T}_{at}$ is the effective radiating temperature of the atmosphere and canopy (K). The outgoing flux is the sum of the radiation emitted by the snow surface and the portion of the incident radiation reflected by the surface. Since the longwave reflectivity of a surface equals one minus its longwave emissivity, we have

$$L_{out} = \varepsilon_{ss} \cdot \sigma \cdot \mathcal{T}_{ss}^{\,4} + (1 - \varepsilon_{ss}) \cdot L_{in}, \qquad \textbf{(5.43)}$$

where the subscript *ss* designates the values of emissivity and temperature for the snow surface.

Combining equations (5.41)–(5.43), expanding and simplifying gives

$$L = \varepsilon_{ss} \cdot \varepsilon_{at} \cdot \sigma \cdot \mathcal{T}_{at}^{\,4} - \varepsilon_{ss} \cdot \sigma \cdot \mathcal{T}_{ss}^{\,4}; \qquad \textbf{(5.44a)}$$

however, since the emissivity of snow is very close to 1 (table 2.1), equation (5.44a) can be simplified to

$$L = \varepsilon_{at} \cdot \sigma \cdot \mathcal{T}_{at}^{\,4} - \sigma \cdot \mathcal{T}_{ss}^{\,4}. \qquad \textbf{(5.44b)}$$

The major problem in applying equation (5.44) is to find expressions for ε_{at} and $\mathcal{T}_{at}$ or, equivalently, to estimate the value of L_{in} under various conditions of cloudiness and forest cover. This problem is addressed in the following sections.

5.5.2.2.1 Clear-Sky Longwave Radiation

Expressions for estimating L_{in} are usually developed by noting that the most important absorbers and emitters of longwave radiation in the atmosphere are carbon dioxide and water vapor (figure 2.4). Since the concentration of carbon dioxide is effectively constant over time periods relevant to snowmelt modeling, variations in the downward flux of longwave radiation under clear skies and no forest canopy are largely due to fluctuations in humidity. Flerchinger et al. (2009) tested the performance of several empirical relations expressing this relation at 21 sites in North America and China, and found the following relation was among those that performed best:

$$L_{in} = \varepsilon_{clr} \cdot \sigma \cdot \mathcal{T}_a^{\,4}, \qquad \textbf{(5.45)}$$

where $\mathcal{T}_a$ is near-surface air temperature (K) and the clear-sky emissivity ε_{clr} is estimated as

$$\varepsilon_{clr} = 0.83 - 0.18 \cdot \exp(-1.54 \cdot e_a),\ e_a > 0.285 \text{ kPa}, \qquad \textbf{(5.46)}$$

where e_a is the near-surface vapor pressure in kPa. [Vapor pressure can be calculated from air temperature and relative humidity via equations (3.9) and (3.12).] Flerchinger et al. (2009) found that adjustment for elevation did not significantly improve estimates of ε_{clr}.

In another recent comparison of methodologies, Abramowitz et al. (2012) found that the best estimates of L_{in} were given by a simple empirical relation:

$$L_{in} = 2.7 \cdot e_a + 0.245 \cdot \mathcal{T}_a - 45.14, \qquad \textbf{(5.47)}$$

where L_{in} is in $\text{MJ/m}^2 \cdot \text{d}$ and e_a is in kPa.

5.5.2.2.2 Effect of Cloud Cover

Clouds are black-body radiators emitting longwave radiation at a rate determined by the cloud-base temperature, and their presence greatly increases the effective emissivity of the atmosphere. Thus under cloudy conditions, the emissivity ε_{sky} will be determined by the degree of cloud cover. Flerchinger et al.'s (2009) review found the following two empirical relations were best at accounting for the effect of clouds:

$$\varepsilon_{sky} = (1 - 0.84 \cdot C) \cdot \varepsilon_{clr} + 0.84 \cdot C \qquad \textbf{(5.48)}$$

and

$$\varepsilon_{sky} = (1 - \mathcal{S}) + \mathcal{S} \cdot \varepsilon_{clr}, \qquad \textbf{(5.49)}$$

where C is fractional cloud cover and $\mathcal{S}$ is the ratio of actual insolation to clear-sky insolation. Surprisingly, however, Abramowitz et al. (2012) found that equation (5.47) performed best for both clear and cloudy conditions, and suggested its use without correcting for clouds.

5.5.2.2.3 Effect of Forest Canopy

Like clouds, trees are very nearly blackbodies with respect to longwave radiation (table 2.1), and they can be considered to be emitting radiant energy at a rate determined by their temperature. Since their temperature is close to the near-surface air temperature, their effect on the total integrated atmospheric emissivity can be modeled as

$$\varepsilon_{at} = (1 - F) \cdot \varepsilon_{sky} + F, \qquad \textbf{(5.50)}$$

where F is fractional forest cover as defined for shortwave radiation.

5.5.2.2.4 Longwave Radiation Emitted by Snow Surface

The second term on the right side of equation (5.44) is the radiation flux emitted by the snow surface. Brubaker et al. (1996) showed that average daily snow-surface temperature is well approximated by

$$\mathcal{T}_{ss} = \min[(\mathcal{T}_a - 2.5), 273.16]. \qquad \textbf{(5.51)}$$

During the ripening and output phases of melting, the snow surface is at the freezing point, $\mathcal{T}_{ss}$ = 273.16 K.

5.5.2.2.5 Summary

When forest cover is absent, values of $\varepsilon_{at} = \varepsilon_{sky}$ as given by equation (5.46) are < 1; however, $\varepsilon_{at} = 1$ for complete forest cover [equation (5.50) with $F = 1$]. Thus from equation (5.44b), L will be positive with $F = 1$ when $\mathcal{T}_a > \mathcal{T}_{ss}$. In most situations, however, $\varepsilon_{at} < 1$ and L is negative.

5.5.2.3 Turbulent Exchange of Sensible Heat

The physics of turbulent exchange of sensible heat were developed in section 3.5.3.6. Combining equations (3.54) and (3.55) gives the flux of sensible heat from the atmosphere into a snowpack, H [E L^{-2} T^{-1}], as

$$H = \frac{0.622 \cdot \kappa^2 \cdot \rho_a \cdot c_p \cdot u(z_m) \cdot \left[T(z_m) - T_{ss}\right]}{\left[\ln\left(\frac{z_m - z_d}{z_0}\right)\right]^2}, \qquad \textbf{(5.52)}$$

where $\kappa = 0.4$, ρ_a is the density of air (≈ 1.292 kg/m^3), c_p is the heat capacity of air ($\approx 1.005 \times 10^{-3}$ MJ/kg · K), z_m is the measurement height above the snow surface, z_d is the zero-plane displacement height, z_0 is the surface-roughness height, $u(z_m)$ is the wind speed, $T(z_m)$ is the air temperature, and T_{ss} is the surface temperature.

To modify this equation for snow, we can assume that z_d is negligibly small. The roughness height, z_0, depends on the irregularity of the snow surface, and so can be highly variable from place to place and with time at a given location. For example, Anderson (1976) measured values between 0.0001 and 0.038 m for his research site in Vermont. However, his data show a strong decrease in z_0 as the season progressed, and values during the melt season did not exceed 0.005 m. In the absence of other information, a value between 0.0005 and 0.005 m may be selected; however, it should be noted that for special situations, such as vegetation projecting above the snow surface or patchy snow, z_0 could be considerably higher.

Assuming that z_m is a standard measurement height (2 m), we designate $T(z_m) = T_a$ and $u(z_m) = u_a$, so that with $c_p = 0.001005$ MJ/kg · K, $\rho_a = 1.29$ kg/m^3, and $z_0 = 0.002$ m, equation (5.52) becomes

$$H = 4.303 \times 10^{-6} \cdot u_a \cdot (T_a - T_{ss}) \text{ MJ/m}^2 \cdot \text{s} \qquad \textbf{(5.53a)}$$

$$H = 0.372 \cdot u_a \cdot (T_a - T_{ss}) \text{ MJ/m}^2 \cdot \text{d} \qquad \textbf{(5.53b)}$$

where u_a is in m/s and temperatures are in °C. Equation (5.53) is analogous to equation (3.55).

There are two additional considerations in the application of equations (5.52) and (5.53). First, as explained in section 3.5.3.7, those equations apply strictly to conditions of neutral atmospheric stability, i.e., when the actual temperature gradient in the air near the surface equals the adiabatic lapse rate. When warm air overlies a snowpack, the actual lapse rate is typically less steep than adiabatic and temperatures may even *increase* with elevation (a "temperature inversion"), so stable conditions exist that tend to suppress turbulent exchange (see figure 3.13). To account for this, the value of H can be adjusted, as explained in box 3.2.

The second consideration in applying equations (5.52) and (5.53) is that wind speeds are virtually always measured in fields or clearings, and such measurements must be adjusted for calculating turbulent exchange in forested areas. Few data are available on which to base an adjustment factor; Dunne and Leopold (1978) suggested the following simple relation:

$$\frac{u_{aF}}{u_{aO}} = 1 - 0.8 \cdot F, \qquad \textbf{(5.54)}$$

where F is the fractional forest cover and the subscripts F and O indicate wind speed in and outside of the forest, respectively. Wang et al. (2010) proposed a relation that depends on temperature, forest-cover fraction, and leaf-area index (LAI):

$$\frac{u_{aF}}{u_{aO}} = \left\{ F \cdot \mathrm{Min}\left(\frac{T_a - T_{ss}}{5}, 1 \right) \cdot [1 - \exp(-LAI)] \right\}^{-1}, \quad \textbf{(5.55)}$$

where Min(.,.) denotes the lesser of the quantities in parentheses.

5.5.2.4 Turbulent Exchange of Latent Heat

Latent-heat exchange with the atmosphere is governed by the same turbulent process that produces sensible-heat exchange; this process is described in section 3.5.3.5 and leads to equation (3.49) for neutral stability:

$$\lambda E = \frac{0.622 \cdot \rho_a \cdot \lambda \cdot \kappa^2 \cdot u(z_m) \cdot [e(z_m) - e_{ss}]}{p \cdot \rho_w \cdot \left[\ln\left(\frac{z_m - z_d}{z_0} \right) \right]^2}, \quad \textbf{(5.56)}$$

where λ is the latent heat of sublimation, ρ_w is density of water, p is atmospheric pressure, $e(z_m)$ is vapor pressure at the measurement height, e_{ss} is the vapor pressure at the snow surface, and the other symbols are as for equation (5.52).

If the vapor-pressure gradient is directed upward [$e(z_m) < e_{ss}$], evaporation/sublimation occurs and latent heat will be lost; if directed downward [$e(z_m) > e_{ss}$] condensation occurs along with an input of latent heat. In applying this equation to snow two phase changes may be involved: For cold snowpacks [$T(0) < 0$°C], evaporation and condensation involve the solid-vapor or vapor-solid phase change (sublimation) and the latent heat involved is the sum of the latent heats of vaporization, λ_v, and fusion, λ_f, so $\lambda = \lambda_v + \lambda_f$. For melting snowpacks [$T(0) = 0$°C], no solid-liquid or liquid-solid phase change occurs and only λ_v is involved.

Again, assuming a standard measurement height, near-surface values of ρ_a, ρ_w, κ, p, $z_d = 0$, and $z_0 = 0.002$ m, $\lambda_v = 2.47$ MJ/kg, $\lambda_f = 0.334$ MJ/kg, equation (5.56) becomes

Cold Snow ($T_{ss} < 0$°C):

$$\lambda E = 6.86\times10^{-5} \cdot u_a \cdot (e_a - e_{ss}) \text{ MJ/m}^2 \cdot \text{s} \quad \textbf{(5.57a)}$$

$$\lambda E = 5.93 \cdot u_a \cdot (e_a - e_{ss}) \text{ MJ/m}^2 \cdot \text{d} \quad \textbf{(5.57b)}$$

Melting Snow ($T_{ss} = 0$°C):

$$\lambda E = 6.05\times10^{-5} \cdot u_a \cdot (e_a - e_{ss}) \text{ MJ/m}^2 \cdot \text{s} \quad \textbf{(5.57c)}$$

$$\lambda E = 5.22 \cdot u_a \cdot (e_a - e_{ss}) \text{ MJ/m}^2 \cdot \text{d} \quad \textbf{(5.57d)}$$

where u_a is the wind speed (m/s) and e_a is the vapor pressure (kPa) at the measurement height. Equation (5.57) is analogous to equation (3.50).

As with the sensible heat, (1) these relations are valid for neutral conditions and may need to be adjusted to account for stability effects (section 3.5.3.7; box 3.2) and (2) equation (5.54) or (5.55) may be appropriate for estimating wind speeds in forests. Note also that values of the numerical coefficients in equations (5.53) and (5.57) change with measurement height and roughness height.

In forests, snow evaporation occurs from the snow intercepted on the canopy, and evaporation from the ground becomes important only after the intercepted snow has disappeared via ablation or falling or blowing off (Lundberg and Halldin 1994). There is evidence that evaporation of intercepted snow may occur at rates of up to 3.3 mm/d and be an important component of the snow ablation in forests, perhaps amounting to 200 mm or more per winter (Lundberg et al. 1998).

5.5.2.5 Heat Input by Rain

When rain falls on a snowpack that is at the freezing point ($T_s = T_{mp}$), the rainwater is cooled to the snow temperature and the heat given up by the water is used in melting. Thus for this situation, we can calculate the heat contributed by rain, R, as

$$R = \rho_w \cdot c_p \cdot r \cdot (T_r - T_{mp}) \quad \textbf{(5.58a)}$$

where c_p is heat capacity of water (4.187×10^{-3} MJ/kg · K), r is rainfall rate [L T^{-1}] and T_r is the temperature of the rain.

When rain falls on snow that is below freezing, it will first cool to the freezing point, giving up sensible heat according to equation (5.58a), and then freeze, liberating latent heat. In this case we have

$$R = \rho_w \cdot c_p \cdot r \cdot (T_r - T_{mp}) + \rho_w \cdot \lambda_f \cdot r. \quad \textbf{(5.58b)}$$

If humidity information as well as air temperature is available, T_r can be estimated as the wet-bulb temperature T_{wb} [equation (5.12)]. However, since relative humidity is usually close to 1 when rain occurs, $T_{dp} \approx T_a$ and $T_{wb} \approx T_a$, so the usual practice is to assume $T_r = T_a$.

5.5.2.6 Conductive Exchange of Sensible Heat with the Ground

Temperatures in the soil under snowpacks usually increase downward due to thermal energy stored during the summer and geothermal heat and the insulating effect of snow. In these circumstances, heat is conducted upward to the base of the snowpack at a rate G given by

$$G = k_G \cdot \frac{dT_G}{dz}, \qquad \textbf{(5.59)}$$

where k_G is the thermal conductivity of the soil [E L^{-1} Θ^{-1} T^{-1}], T_G is soil temperature, and z is distance below the ground surface.

Thermal conductivities of soils depend on soil texture, soil density, and moisture content and vary widely spatially and temporally. For example, the US Army Corps of Engineers (1956) reported a more than tenfold increase in k_G during the melt season in the soil they studied, from 8.37×10^{-3} to 0.100 MJ/m · d. This variability, along with the general lack of information about thermal conductivity and ground-temperature gradients, often precludes accurate computation of G. This usually has little practical effect on energy-balance estimates during the snowmelt season, however, because G is usually negligible compared to other terms.

In spite of its generally negligible contribution during the melt season, the energy conducted to the snowpack from the ground during the accumulation season can be hydrologically significant: Studies from various localities (Federer and Lash 1978a; Male and Gray 1981) indicate that this heat produces continual melting at the base of the snowpack, called **groundmelt**, at rates up to 2 mm/d (a heat input of 0.668 MJ/m^2 · d). Groundmelt can add significantly to moisture in the soil, increasing the percentage of snowmelt that will runoff during the snowmelt season, and, in regions like New England, groundmelt may be the principal source of flow in upland streams during the winter.

5.5.3 Relative Importance of Energy-Balance Terms

5.5.3.1 Effects of Forest Cover and Weather

We can use the relations developed in section 5.5.2 to explore the relative importance of the energy-balance components under various conditions of forest cover and weather. As an example, we specify a ripe snowpack on a horizontal location at latitude 45°N on 21 March. Using the relations in appendix D, which are incorporated in the SolarRad.xls program found on the disk accompanying this text, the daily clear-sky solar-radiation input is calculated to be K_{CSh} = 16.721 MJ/m^2 · d.

To emphasize contrasts, we will use energy-balance computations at two sites for two forest-cover conditions as an example. At site 1, F = 0; at site 2, F = 1. Both sites will be compared under two sets of weather conditions. Condition A is a clear day with low humidity and no rain (C = 0, RH = 0.7, r = 0 mm/d) and condition B is a cloudy day with high humidity and heavy rain (C = 1, RH = 1, r = 25 mm/d). For all conditions we assume air temperature T_a = 4°C, wind speed in the open is u_{aO} = 3 m/s, albedo a = 0.5 (typical for an 8-day-old snow surface; figure 5.22), and a constant ground-heat input of G = 0.25 MJ/m^2 · d.

The calculations have been carried out using the SnowMelt.xls program on the accompanying disk using the relations developed in section 5.5.2. Stability adjustments were made as described in box 3.2. The results are shown in table 5.4. Note that by far the highest energy input and melt occur at the open site under cloudy, rainy, and humid conditions when the dominant energy input is latent heat from condensation ("condensation melt"). The second highest input occurs under similar conditions at the forested site, when latent-heat input also dominates. Note that the rain, even though a relatively large amount, contributes only minor heat input at both sites. Solar radiation is the largest input only at the open site under clear skies, but this is balanced by heat loss due to longwave radiation and latent heat.

Note that the relative importance of the solar-radiation term would be much greater on south-facing slopes, and much less on north-facing slopes, than shown in table 5.4, but the other terms would not be affected by slope and aspect. This largely explains why the largest snowmelt floods are usually due to condensation melt, which occurs quasi-uniformly on all slopes and is less affected by forest cover than are solar and longwave radiation.

5.5.3.2 Case Study of Snowmelt at Danvillle, Vermont

During a typical winter (1972–1973), the NWS, in conjunction with the USDA's Agricultural Research Service, measured the accumulation and melt of a snowpack at the Sleepers River Research Watershed in Danville, Vermont (figure 5.23 on p. 236). Although average snowpack temperature was not measured, the

beginnings and ends of the accumulation period and the phases of the melt period can be approximated from the traces of depth, average snowpack density, water equivalent, and average air temperature.

Air temperature was above 0°C only occasionally between mid-November and late February, and the water equivalent of the pack increased more or less continually during this period due to snowfalls and minor rain. The maximum snow depth of 72 cm was reached in late February. Density was initially about 100 to 150 kg/m^3, jumped to about 250 kg/m^3 in early December, and increased gradually thereafter to about 300 kg/m^3 when the melt season began. Density increases were due largely to constructive metamorphism and occasionally to refreezing at depth of rain and surface melt.

The accumulation period ended when air temperature began a final rise on 26 February; temperature was above freezing from 4 to 17 March, and water equivalent began to decline on 4 March. Significant water output was measured in a snowmelt lysimeter from 9 through 18 March. Density climbed from about 300 kg/m^3 to 400 kg/m^3 during the first two phases of melt; it then fluctuated between 350 and 450 kg/m^3 and eventually reached 520 kg/m^3 just before melting was complete.

Table 5.5 on p. 237 gives the amounts of energy involved in each of the components of the energy budget during the accumulation and melt periods for six seasons at the Danville site. For all accumulation seasons, L was negative and more than balanced K, resulting in negative net radiation. H was positive and LE negative in all accumulation seasons, but the magnitude of H was several times greater than that of LE, so there was a net input of heat from turbulent exchange. There was a very small contribution from rain. The overall positive net input is largely due to ground heat, which was sufficient to produce about 87 mm of groundmelt.

In all melt seasons, the input from K was about twice the loss via L, resulting in a strongly positive net radiation. This was augmented slightly by G and negligibly by R. Again, sensible-heat exchange was positive and latent-heat exchange negative, but of considerably

Table 5.4 Example Energy-Balance Computations Using Relations of Section 5.5.2.

Conditions	Site 1 Condition A	Site 1 Condition B	Site 2 Condition A	Site 2 Condition B
F	0.00	0.00	1.00	1.00
C	0.00	1.00	0.00	1.00
T_a (°C)	4.00	4.00	4.00	4.00
RH	0.70	1.00	0.70	1.00
u_{aO} (m/s)	3.00	3.00	3.00	3.00
R (mm/d)	0.00	25.00	0.00	25.00
a	0.50	0.50	0.50	0.50
Energy-Balance Terms (MJ/m^2 · d)				
K	8.65	2.97	0.17	0.06
L	–3.28	0.85	1.63	1.63
$K + L$	5.37	3.81	1.81	1.69
H	4.43	4.43	0.89	0.89
LE	–6.99	34.4	–1.40	6.87
R	0.00	0.42	0.00	0.42
G	0.25	0.25	0.25	0.25
F_E	3.07	43.3	1.55	10.1
Water Production (mm/d)				
Snowmelt	9.2	129.6	4.6	30.3
Total ablation	12.0	129.6	5.2	30.3
Snowmelt + Condensation + Rain	9.2	168.4	4.6	58.1

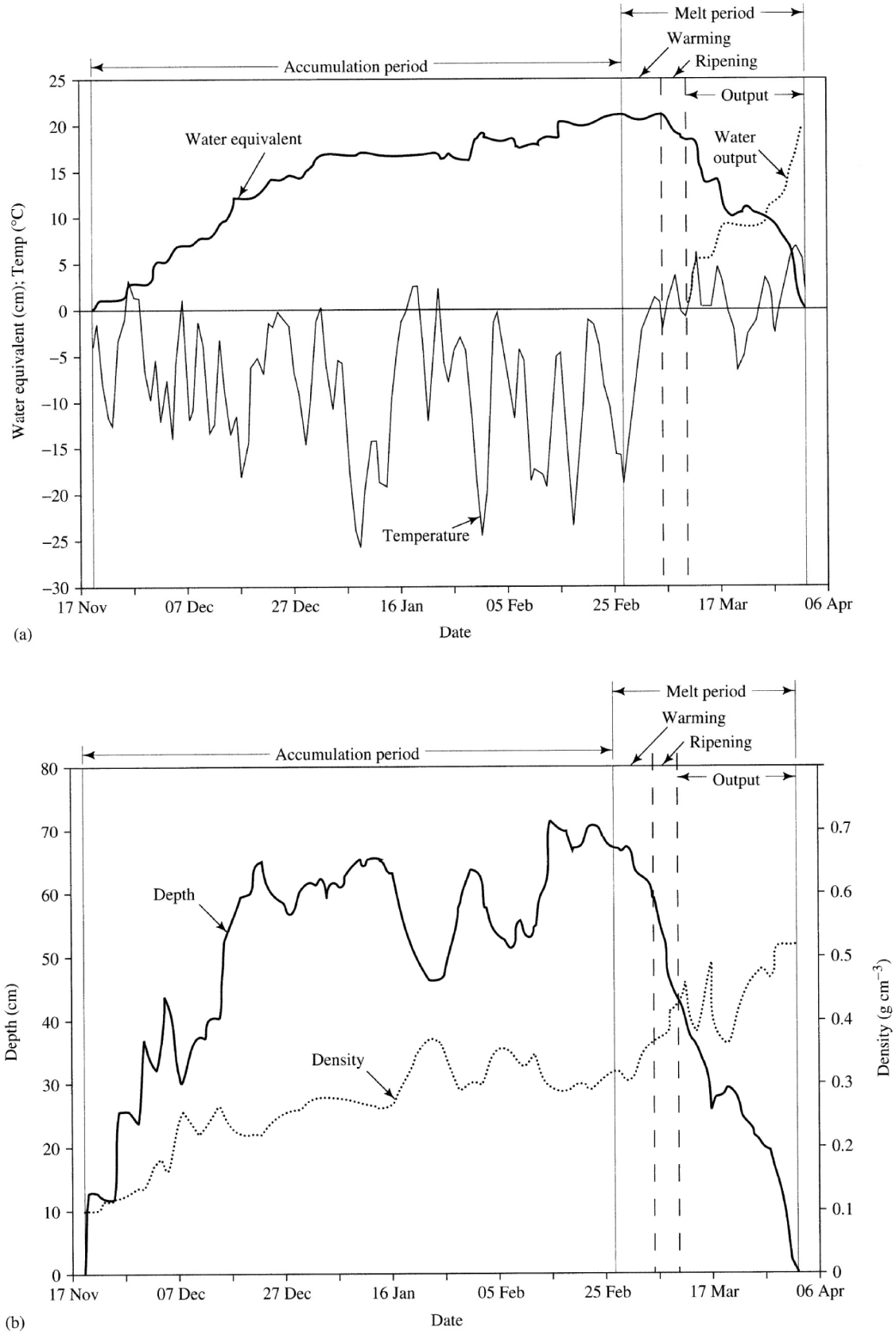

Figure 5.23 (a) Snowpack water equivalent, average air temperature, and cumulative water output and (b) snowpack depth and density at the Sleepers River Research Watershed in Danville, Vermont, for 1972–1973. The accumulation period and three phases of the melt period are shown; the boundary between the warming and ripening phases is uncertain [data from Anderson et al. (1977)].

Table 5.5 Energy-Balance Components (MJ/m^2) for Six Seasons at the NWS Snow Research Station, Danville, Vermont.

	68–69	69–70	70–71	71–72	72–73	73–74	Average
				Accumulation Season			
Net shortwave radiation, *K*	167.94	171.50	195.28	169.70	115.14	191.76	168.55
Net longwave radiation, *L*	–264.49	–259.64	–282.87	–238.95	–174.39	–225.85	–241.03
Net radiation, *K* + *L*	–96.55	–88.14	–87.59	–69.25	–59.25	–34.08	–72.48
Heat from rain, *R*	0.08	0.84	0.25	0.38	0.71	1.00	0.54
Heat from ground, *G*	30.77	53.89	32.24	25.00	26.29	29.73	32.99
K + *L* + *R* + *G*	–65.69	–33.41	–55.10	–43.88	–32.24	–3.35	–38.95
Turbulent exchange, sensible, *H*	96.76	84.37	112.92	92.49	65.40	81.86	88.97
Turbulent exchange, latent, *LE*	–11.97	–25.88	–27.13	–24.45	–16.08	–20.39	–20.98
H + *LE*	84.79	58.49	85.79	68.04	49.32	61.47	67.98
Net heat input, F_E	19.09	25.08	30.69	24.16	17.08	58.12	29.04
				Melt Season			
Net shortwave radiation, *K*	191.97	129.00	162.83	150.73	149.69	168.78	158.83
Net longwave radiation, *L*	–101.12	–67.49	–77.29	–74.78	–92.45	–109.99	–87.19
Net radiation, *K* + *L*	90.86	61.51	85.54	75.95	57.24	58.79	71.65
Heat from rain, *R*	0.46	0.63	0.71	1.26	0.67	1.17	0.82
Heat from ground, *G*	5.23	3.56	5.07	4.27	9.55	9.30	6.16
K + *L* + *R* + *G*	96.55	65.69	91.32	81.48	67.45	69.25	78.62
Turbulent exchange, sensible, *H*	66.57	43.13	67.12	65.86	56.32	60.80	59.96
Turbulent exchange, latent, *LE*	–28.35	–17.88	–23.66	–28.85	–35.00	–31.90	–27.61
H + *LE*	38.23	25.25	43.46	37.01	21.31	28.89	32.36
Net heat input, F_E	134.78	90.94	134.78	118.49	88.76	98.14	110.98

Source: Anderson (1976).

smaller magnitude, giving a net input from turbulent-exchange processes. The positive net heat input for melt seasons is the energy used in melting.

5.5.3.3 Comparison of Energy Balances in Different Environments

Kuusisto (1986) reviewed over 20 studies of melt-period energy balances; his summary is given in table 5.6. The comparable information for Anderson's (1976) study (computed for the melt season from table 5.5) has been added. Kuusisto (1986) made the following generalizations based on his survey:

- Net radiation and turbulent exchange play a major role in the energy balance, and heat from rain and from the ground are small or negligible.
- Net radiation and sensible-heat exchange are positive during snowmelt in most locations.
- Latent-heat exchange is positive in some places, but negative in others. This is likely the result of contrasting humidity and wind conditions.
- The net radiation is the most important component in forests, probably due to the less-negative or positive longwave radiation and reduced windspeeds.
- On cloudy or rainy days, turbulent exchange of latent heat dominates.
- Very high areal snowmelt rates are usually caused by intense positive turbulent heat exchange under humid, windy, and warm conditions.

This last generalization has important implications for forecasting conditions that can cause snowmelt flooding. Very warm, humid air and high winds above a ripe snowpack can produce very high rates of melt due to latent-heat input. The potential for

Table 5.6 Relative Contributions of Energy-Balance Components to Snowmelt in Different Environments[a]

Study	Site[b]	Period[c]	Percent Contribution from				
			K + L	*H*	*LE*	*R*	*G*
1	Open field, CA, 37°N		72	28	–18		
2	Open field, Canada, 45°N (100 m)	Mar 59 (0.7)	75	25	–74		
3	Open field, AK, 67°N	Mar–Apr 66	86	14	24		
4	Open field in mts., CA, 37°N	Apr–May 47–51 (daytime)	73	23	4		
5	Open field, MI, 46°N	23 Jan 69 (1.5)	17	47	36		
6	Forest opening, CO, 39°N (3,260 m)	Jun 68 (5.0)	56	44	–3	0	
7	Open field in mts., France, 46°N (3,550 m)	Jul 68 (1.6)	85	15	–15		
8	Open field in mts., Spain, 41°N (1,860 m)	Apr 70 (1.0)	100	–11	–42		
9	Open field, AK, 71°N (10 m)	Jun 71	100	–19	–10		–22
10	Open field in prairie, Canada, 51°N	Melt season 74 (0.8)	59	41	–10		–6
11	Open field in prairie, Canada, 51°N	Melt season 75 (0.5)	95	5	–29		–1
12	Open field in prairie, Canada, 51°N	Melt season 76 (0.3)	67	33	–14		–4
13	Deciduous forest, Ontario, 46°N	Apr 78 (1.0)	100	0	0		
14	Open field, Finland (60 m)	Melt seasons 68–73 (0.7)	46	53	–4	1	
15	Open field in mts., Norway, 60°N	Apr–May 79–80 (1.2)	35	65	0		
		cloudy days (2.3)	20	54	26		
		clear days (0.7)	37	63	–24		
16	Small basin, 23% forest, Switzerland, 47°N (800 m)	Days with intense snowmelt, 77–80 (2.3)	8	65	20	7	
17	Open field, AK, 65°N	Apr 80 (0.3)	67	33	–68		0
18	Open field, Finland, 61°N	Days with intense snowmelt, 59–78 (1.4)	48	47	2	3	
19	Open field, Finland, 67°N	Days with intense snowmelt, 59–78 (1.5)	58	40	–23	2	
20	Open tundra, NWT, Canada, 79°N (200 m)	Melt seasons 69–70	100	–90	–77		–45
21	Open field in mts., New Zealand, 43°S (1,500 m)	Oct–Nov 76–80	30	57	13	< 1	
		Rainy days	17	55	25	3	
		Days with greatest heat input	16	60	23	1	
22	Open field in mts., New Zealand, 43°S (1,450 m)	Melt season 82 (3.1)	16	57	25	2	
23	Open field, WI, 3 sites, 43–45°N	Melt seasons 53–64	–31	100	–12		
24	Small basin, 82% forest, Finland 64°N (120 m)	Melt seasons 71–81 (0.5)	86	14	–13	< 1	
25	Open field, hilly area, VT, 45°N (550 m)	Melt seasons 69–74 (1.3)	52	43	–20	< 1	4

[a] 100% is the sum of all positive components.
[b] Number in parentheses is site elevation.
[c] Number in parentheses is average melt in cm/d.

Sources: Data from Kuusisto (1986): see that paper for references to individual studies. Data from Anderson (1976) added as study 25.

flooding under these conditions is high because this situation would typically exist generally over a watershed, whereas rapid melting due to solar radiation is largely restricted to south-facing, nonforested slopes. When rain accompanies warm winds, the flooding potential may be further exacerbated by the rain to produce a "rain-on-snow event," which is common in the western United States (McCabe et al. 2007) and elsewhere (Sui and Koehler 2001), and which generated the record floods of March 1936 in central New England. As can be seen in tables 5.4–5.6, the heat introduced by the rain plays only a small role in generating melt; but in some cases the rain itself, with little melt, can produce floods (Singh et al. 1997).

One severe flooding case in which melt due to solar radiation did play a large role was that of the Red River in North Dakota and Minnesota in the spring of 1997. The watershed of the Red River is flat and largely unforested; the flood severity was exacerbated because of a record snowpack, the fact that the river flows northward, and the interruption of the melt season by a major blizzard (Macek-Rowland 1997).

5.6 Snowmelt Runoff Generation

We saw earlier that a ripe snowpack typically retains only a small fraction of its water equivalent as liquid water, which is present as thin films held by surface tension occupying less than 10% of the pore space (figures 5.15 and 5.16). As additional water is produced during the last phase of melting it can no longer be held against gravity, and downward percolation begins. Natural snowpacks are seldom homogeneous, and usually contain discontinuous layers of varying density that temporarily store and horizontally divert the percolating water (Marsh and Woo 1985; Conway and Benedict 1994; Hirashima et al. 2010). Figure 5.24 shows that the distribution of liquid water in a melting snowpack is far from uniform vertically or horizontally. However, ice layers usually disappear as melt progresses, and melting snowpacks tend to become fairly uniform assemblages of quasi-spherical grains of 1 to 3 mm diameter. Thus to gain a basic understanding of the physical processes involved we can treat melting snowpacks as *homogeneous porous media*, physically identical to coarse-grained soils.

Water arriving at the bottom of the snowpack infiltrates into the soil and/or accumulates to form a saturated zone at the base of the snowpack, moving toward a surface-water body by one of the paths illustrated in figure 5.25. In figure 5.25a, the water table is at depth and the ground above it is unsaturated, so all of the water output infiltrates and moves streamward as subsurface flow. In figure 5.25b, the infiltration rate is less than the water-output rate, so a basal saturated zone develops within the snowpack through which water flows toward the stream. In figure 5.25c, ground conditions are simi-

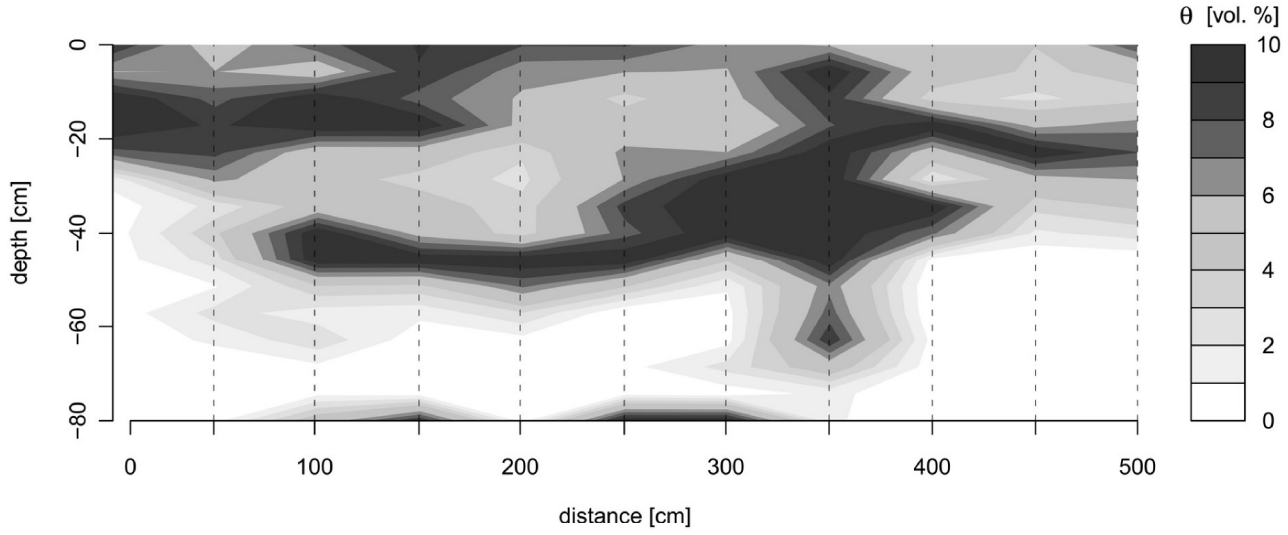

Figure 5.24 Contour plot showing cross section of snow wetness (θ) to a depth of 80 cm over 5-m wide areas across a slope in the Swiss Alps in the early stages of snowmelt [Techel and Pielmeier (2011)].

lar to those of 5.25a, but the water table has risen above the ground surface on the lower part of the slope so that water moves streamward by both surface and subsurface routes.

The process of infiltration will be discussed in detail in chapter 8, and runoff generation by processes similar to those shown in figure 5.25c will be examined in chapter 10. Here we focus on snowmelt-runoff generation by the process shown in figure 5.25b, following Dunne et al. (1976) (figure 5.26).

5.6.1 Flow in the Unsaturated Zone

Above any basal saturated zone, which may form where meltwater accumulates at an ice layer or at the ground surface, the pores of snowpacks are only partially filled with liquid water. Thus the vertical percolation of water in the snowpack is a form of *unsaturated porous-media flow*, which is governed by the basic law of flow in porous media, *Darcy's law* (discussed in detail in section 7.3). Colbeck (1974,

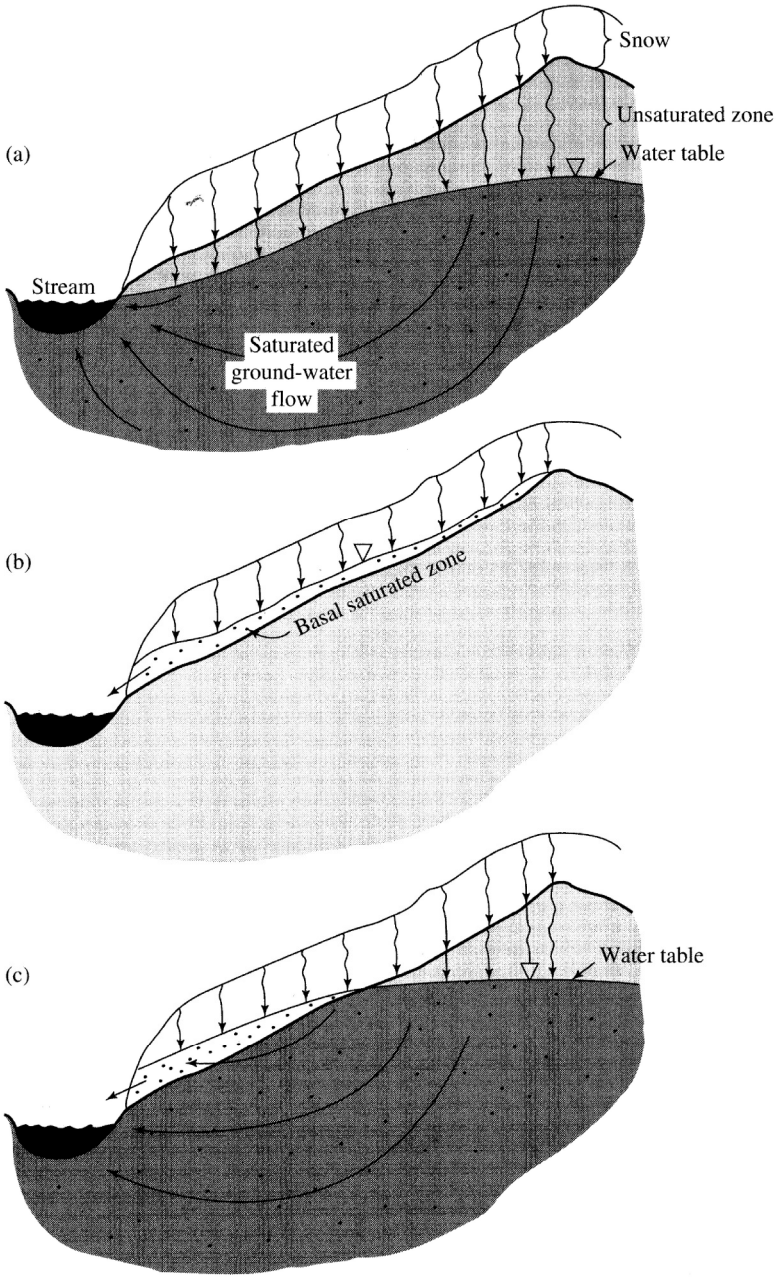

Figure 5.25 Three modes of snowmelt-runoff generation. (a) The top of the saturated zone in the soil (water table) is at depth; percolating meltwater infiltrates and percolates to the saturated zone to raise the water table and thereby induce increased ground-water flow to the stream. (b) The water table is at the soil surface or the soil surface is impermeable (perhaps due to solid soil frost); percolating meltwater accumulates to form a basal saturated zone through which water drains to the stream. (c) The lower portion of the water table has risen above the ground surface into the snowpack; water in the upper part of the slope moves as in (a), water in the lower part as in (b) [adapted from Dunne and Leopold (1978)].

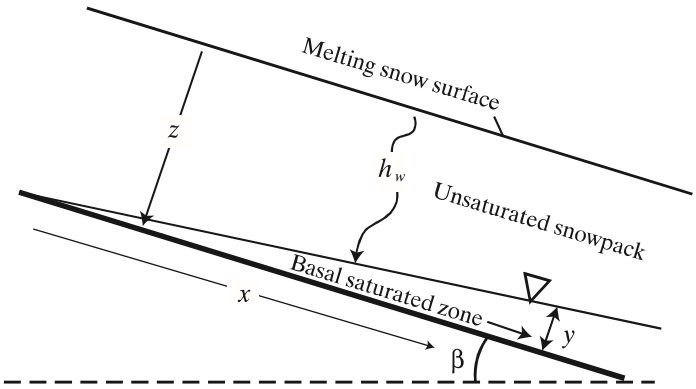

Figure 5.26 Definition diagram for snowmelt runoff processes.

1978) gave a detailed description and experimental validation of the application of Darcy's law to snowmelt percolation, and his treatment is followed here.

Because of the relatively large grain sizes, surface-tension forces in snow are usually negligible in relation to gravitational forces. Thus Darcy's law can be simplified to

$$q_z = K_{hun}, \tag{5.60}$$

where q_z is the downward vertical flux rate (volume of water per unit horizontal area per unit time [L T^{-1}]) and K_{hun} is the **unsaturated hydraulic conductivity** of the snow [L T^{-1}]. As in soils, unsaturated hydraulic conductivity is a function of the **saturated conductivity**, K_h, and the degree to which the pores contain water;

$$K_{hun} = K_h \cdot S^c, \tag{5.61}$$

where S is the fraction of pore space containing mobile water,

$$S \equiv \frac{\theta_w - \theta_{ret}}{\phi - \theta_{ret}}, \tag{5.62}$$

and the exponent has been found experimentally to be $c \approx 3$. K_h in turn is a function of snow density (inversely related to pore-space size) and grain size, d, and can be estimated as

$$\begin{aligned} K_h &= 0.077 \cdot d^2 \cdot (g/\nu) \cdot \exp(-7.8\times10^{-3} \cdot \rho_s) \\ &= 4.4\times10^5 \cdot d^2 \cdot \exp(-7.8\times10^{-3} \cdot \rho_s), \end{aligned} \tag{5.63}$$

where K_h is in m/s, d is in m, g is gravitational acceleration (9.81 m/s^2), ν is kinematic viscosity of water at 0°C (1.79×10^{-6} m^2/s), and ρ_s is snow density in kg/m^3 (Shimizu 1970; Hirashima et al. 2010). Combining equations (5.60)–(5.62),

$$q_z = K_h \cdot S^3 = K_h \cdot \left(\frac{\theta_w - \theta_{ret}}{\phi - \theta_{ret}} \right)^3. \tag{5.64}$$

Energy inputs to the surface of a ripe snowpack vary diurnally, usually approximating a sine curve with a peak input in the early afternoon. Thus the rate of meltwater production (assumed to originate at the surface) varies continually. This variation generates a daily wave of meltwater originating near the surface and percolating downward (figure 5.27). We designate the melt rate at any instant $h_w(t)$, and a given melt rate travels vertically downward at a rate

$$\left. \frac{dz}{dt} \right|_{h_w(t)} = \left(\frac{c}{\phi \cdot (1 - \theta_{ret})} \right) \cdot K_{hun}^{1/c} \cdot h_w(t)^{(c-1)/c}. \tag{5.65}$$

Because the speed of these melt waves increases as the melt rate increases, percolating water produced during the period of peak melting near midday overtakes water produced earlier in the day. Thus the waves tend to accumulate water and develop a sharp wave front, as in figures 5.27 and 5.28. Equation (5.65) can be integrated to show that the depth of penetration, z, of a flux of meltwater with constant flux rate is linearly related to time t:

$$z = \left(\frac{c}{\phi \cdot (1 - \theta_{ret})} \right) \cdot K_{hun}^{1/c} \cdot h_w(t)^{(c-1)/c} \cdot t. \tag{5.66}$$

An example calculation of the travel time of water generated at a particular melt rate is given in box 5.3 on p. 243. To illustrate the overall melt-percolation phenomenon, we use the results of Dunne et al. (1976) over two days of snowmelt at their experimental site at Schefferville, Quebec, Canada. With their measured values, equation (5.66) becomes

$$z = 0.59 \cdot h_w(t)^{2/3} \cdot t, \tag{5.67}$$

where z is in m. Figure 5.29 on p. 243 shows the downward percolation of various melt rates as given by equation (5.67): higher melt rate waves travel

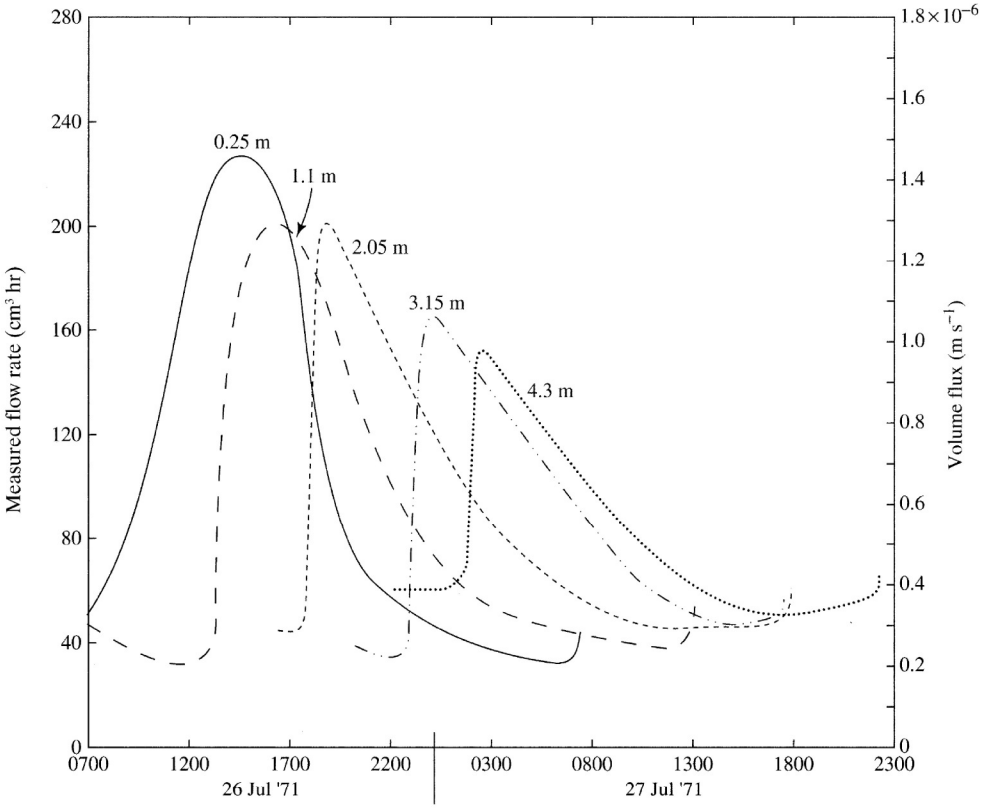

Figure 5.27 Volume rates of flow at different depths in a homogeneous snowpack produced by a day of intense fair-weather melting [Colbeck (1978)].

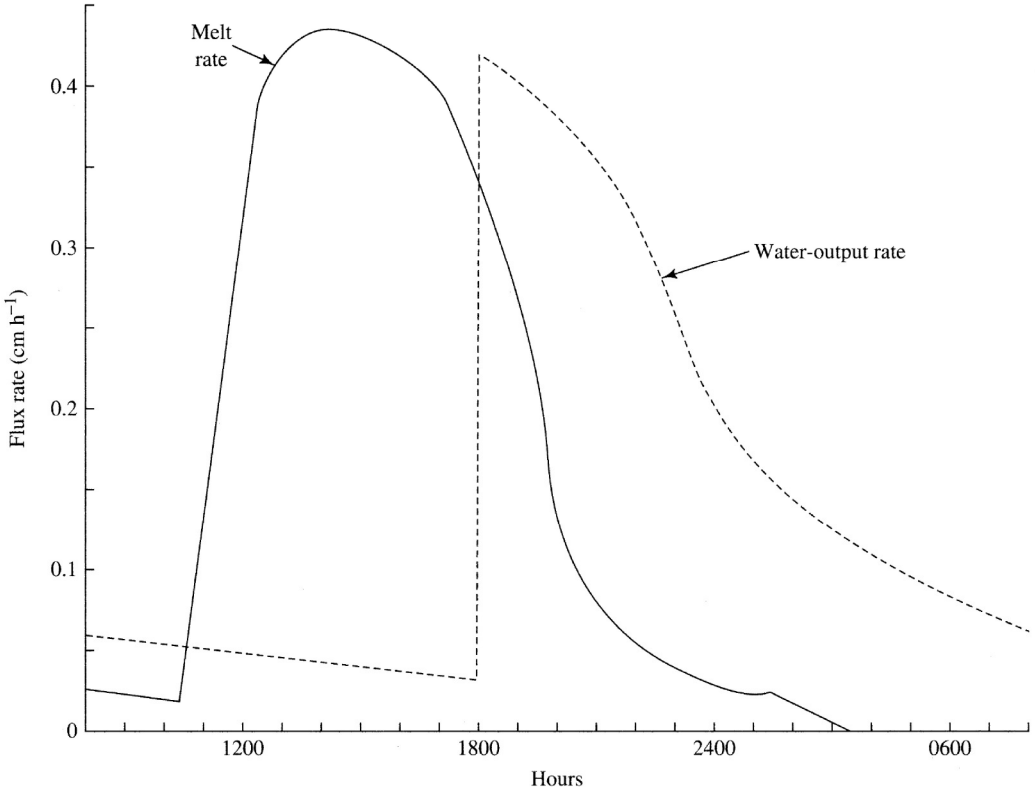

Figure 5.28 Comparison of timing of rate of melting at the surface (the "input") and rate of vertical unsaturated flow at the base of a 101-cm deep tundra snowpack (water output) [Dunne et al. (1976). The generation of runoff from subarctic snowpacks. *Water Resources Research* 12:675–694, with permission of the American Geophysical Union].

Box 5.3 Example Computation of Meltwater Percolation

Consider a ripe snowpack with a depth $h_s = 1.00$ m, a density $\rho_s = 400$ kg/m^3, and a grain size $d = 2$ mm. Then from equation (5.63),

$$K_h = \left(4.4\times10^5 \text{ m/s}\right)\cdot(.002 \text{ m})^2 \cdot \exp\left(-7.8\times10^{-3}\cdot 400 \text{ kg/m}^3\right) = 7.77\times10^{-2} \text{ m/s}. \quad \textbf{(5B3.1)}$$

From equation (5.25),

$$\theta_{ret} = 3\times10^{-10}\cdot 400^{3.23} = 0.076. \quad \textbf{(5B3.2)}$$

From equation (5.5),

$$\phi = 1-\frac{\rho_s-\theta_w\cdot\rho_w}{\rho_i} = 1-\frac{400 \text{ kg/m}^3 - 0.076\cdot\left(1{,}000 \text{ kg/m}^3\right)}{917 \text{ kg/m}^3} = 0.647 \text{ kg/m}^3. \quad \textbf{(5B3.3)}$$

Equation (5.65) then gives

$$\left.\frac{dz}{dt}\right|_{h_w(t)} = \left(\frac{3}{0.647\cdot(1-0.076)}\right)\cdot \left(7.77\times10^{-2} \text{ m/s}\right)^{1/3}\cdot\left[h_w(t) \text{ m/s}\right]^{2/3} = 2.14\cdot h_w(t)^{2/3} \text{ m/s}. \quad \textbf{(5B3.4)}$$

Dunne et al. (1976) measured mid-day melt rates of around $q_z = 0.400$ cm/hr $= 1.11\times10^{-6}$ m/s. Equation (5B3.4) gives the percolation velocity of water generated at this rate as

$$\left.\frac{dz}{dt}\right|_{h_w(t)} = 2.14\cdot\left(1.11\times10^{-6}\right)^{2/3} = 2.3\times10^{-4} \text{ m/s}. \quad \textbf{(5B3.5)}$$

At this velocity, it takes

$$\frac{1 \text{ m}}{2.3\times10^{-4} \text{ m/s}} = 4{,}356 \text{ s} = 1.21 \text{ hr} \quad \textbf{(5B3.6)}$$

for this water to reach the bottom of the snowpack.

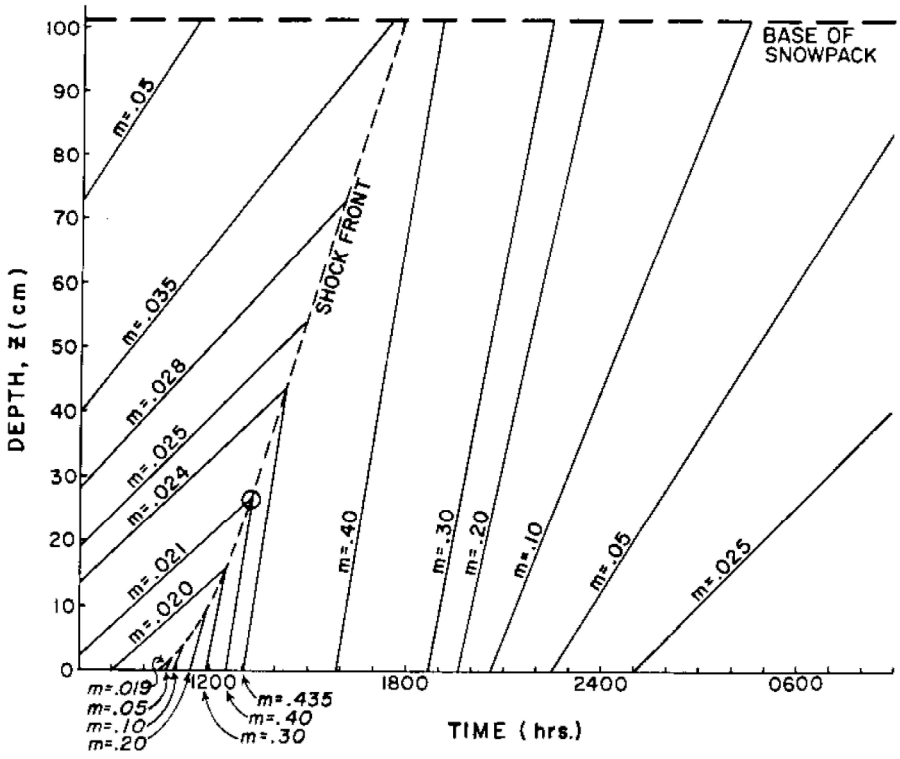

Figure 5.29 Downward percolation of various melt rates ($m \equiv dz/dt$, cm/hr) as given by equation (5.67). The times at which these flux rates intersect the base of the snowpack determines the hydrograph of the input to the saturated layer [Dunne et al. (1976). The generation of runoff from subarctic snowpacks. *Water Resources Research* 12:675–694, with permission of the American Geophysical Union].

faster (steeper curves), and faster-moving waves overtake earlier-generated slower waves to form a shock front (dashed line), which travels at an intermediate speed.

The shock wave in figure 5.29 takes about 7 hr to reach the base of the 1.01-m deep snowpack, so its speed is 0.14 m/hr; the peak of the wave in figure 5.27 moves at a velocity of 0.2 to 0.3 m/hr, and Anderson (1968) found average time lags of ~0.35 m/hr (figure 5.30). Thus for most shallow seasonal snowpacks, the peak water output will occur within a few hours of the peak melt rate. Anderson (1973) developed an empirical expression for the time lag of snow melt, i.e., the elapsed time between the beginning of daily melt and the beginning of water output:

$$\Delta t = 5.33 \cdot \left[1.00 - \exp\left(- \frac{0.03 \cdot h_{swe}}{\Delta h_{w6}} \right) \right], \qquad \textbf{(5.68)}$$

where Δt is the time lag (hr), h_{swe} is the water equivalent of the snowpack when melt begins (m), and Δh_{w6} is the amount of melt generated in a 6-hr period (m).

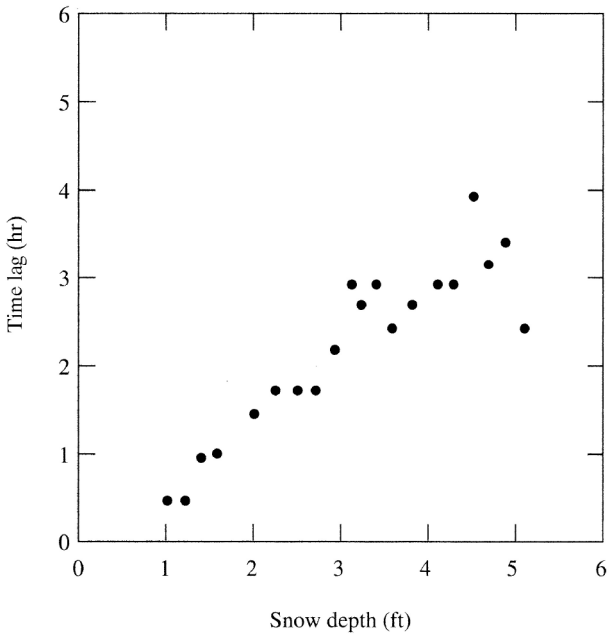

Figure 5.30 Approximate time lag between the time of peak surface melting and the time of peak flow from the bottom of a snowpack as a function of snow depth [Anderson (1968). Development and testing of snow pack energy balance equations. *Water Resources Research* 4:19–37, with permission of the American Geophysical Union].

5.6.2 Flow in the Basal Saturated Zone

Assuming a constant snow depth and uniform conditions above it, the daily wave of water output arrives at the base of the snowpack at the same time all along the slope. This input produces daily waves that travel downslope in the basal saturated zone at a velocity, U_s, where

$$U_s = \frac{K_h}{\phi - \theta_{ret}} \cdot \tan(\beta), \qquad \textbf{(5.69)}$$

K_h is the saturated hydraulic conductivity of the basal snow layer, and β is the slope angle. K_h is estimated via equation (5.63). However, it should be noted that the size of snow grains in the saturated zone can be significantly larger than that in the unsaturated zone due to more rapid metamorphism: For a subarctic snowpack, Dunne et al. (1976) found d = 6 mm in the basal saturated zone and d = 2 mm in the unsaturated zone.

Using the wave velocity U_s, one can calculate the average time of travel of water in the basal saturated zone, t_s, as

$$t_s = \frac{X}{U_s} = \frac{X \cdot (\phi - \theta_{ret})}{K_h \cdot \tan(\beta)}, \qquad \textbf{(5.70)}$$

where X is the slope length. t_s is typically on the order of 1% of the travel time through the unsaturated zone (Male and Gray 1981). Thus where a basal saturated zone forms, the lag time between peak melt rates and peak inputs to small upland streams is determined largely by the travel time associated with the vertical percolation through the snowpack and is typically on the order of several hours. In contrast, infiltrating snowmelt that percolates through the soil to the ground water (figure 5.25a) may not appear in streamflow for months (Bengtsson 1988).

5.7 Snowmelt Modeling

5.7.1 Importance of Modeling

Snow is a critical water resource in many regions, and the extent and depth of snow cover are major influences on energy and water balances. Because of difficulties in accessing remote regions, especially mountainous areas, and limited resources for obtaining ground measurements, satellite observations are widely used for assessing the extent and water equivalent of snow cover. However, interpretation of both optical and passive microwave satellite observations

is far from straightforward, particularly in forested areas. Thus modeling of snow accumulation and melt is an essential tool for water-resource management, simulating global climate, and weather forecasting.

5.7.2 Approaches to Snowmelt Modeling

5.7.2.1 Energy-Balance Approach

The energy-balance relations discussed in section 5.5 form the basis for one class of models of snowmelt at a point. These models are often characterized as "physically based" because the energy balance is a fundamental physical principle (conservation of energy) and because they use equations that describe the physics of processes in each component of the energy balance. However, different models use different representations of these processes, which may be simpler or more complex than described in section 5.5. For example, some models may consider the visible and near-infrared portions of the solar spectrum separately, use different ways of characterizing forest effects on wind and/or snow interception, and consider different layers within the snowpack. Furthermore, the processes can be modeled at different spatial and temporal discretizations; for example, the JULES model described by Parajka et al. (2010a) operates at an hourly time step and a spatial resolution of 25 km × 25 km, and each grid cell contains a variable fraction of nine surface-vegetation types, each of which can be set to have different properties.

Anderson (1976) made a thorough and extensive study and testing of point snowmelt-modeling techniques in a large clearing at an elevation of 550 m in Danville, Vermont, over a period of six years. He found only minor differences in results using time steps of 1, 3, and 6 hr. Maximum time steps should probably not exceed 12 hr in order to capture the drastic differences between daytime and nighttime energy balances. Anderson (1976) also compared model results using snowpack-depth increments of 1, 2.5, 5, and 10 cm, and found that predicted water equivalent at a given time increased as the thickness increased because the thicker layers introduced distortions in the diurnal warming-cooling cycles. Although there is little further evidence on which to base definitive guidelines, one could probably expect significant distortions to appear in energy-balance models using thicknesses exceeding 50 to 100 cm. However, many models treat the snowpack as a single layer.

Andreadis et al. (2009) gave a fairly detailed description of a modern energy-balance-based snow model, others are described by Cline (1997), Melloh (1999), and Wang et al. (2010).

5.7.2.2 Temperature-Index Approach

The empirical **temperature-index approach** to snowmelt modeling was developed because (1) measurements of the many variables required for energy-balance computations are commonly unavailable and (2) the computational resources to implement energy-balance computations are limited. Although the second reason is rapidly becoming less of an issue, some current models use the approach (Rutter et al. 2009).

The temperature-index approach estimates snowmelt, Δw, for a time period as a linear function of air temperature:

$$\Delta w = M \cdot (T_I - T_b),\ T_I \geq T_b;$$
$$\Delta w = 0,\ T_I < T_b, \qquad \textbf{(5.71)}$$

where M is a **melt coefficient** (or **melt factor** or **degree-day factor**), T_I is an **index temperature**, and T_b is a **base temperature**. The base temperature used is almost always the melting point, 0°C, and the index temperature is the average or maximum temperature for the time period.

This approach is justified because the snow-surface temperature is at or near 0°C during melting, energy inputs from longwave radiation and turbulent exchange are approximately linear functions of air temperature, and there is a general correlation between insolation and air temperature. Figure 5.31 shows that equation (5.71) approximates daily melt at the Danville, Vermont, snow research site—although there is considerable scatter. The value of M that best fits these data is $M = 3.6$ mm/d · °C, and the intercept value, −1.4 mm/d, is not significantly different from 0.

The value of M varies with latitude, elevation, slope inclination and aspect, forest cover, and time of year, and should ideally be empirically determined for a given watershed. In the absence of site-specific data, several studies have suggested generalized approaches to estimating M (table 5.7).

5.7.2.3 Hybrid Approach

The dependence of the melt factor on time of year, land cover, and slope factor (table 5.7) largely reflects the importance of solar radiation on snowmelt. To reduce this variability and improve prediction accuracy while retaining practical data requirements, Kustas et al. (1994) and Brubaker et

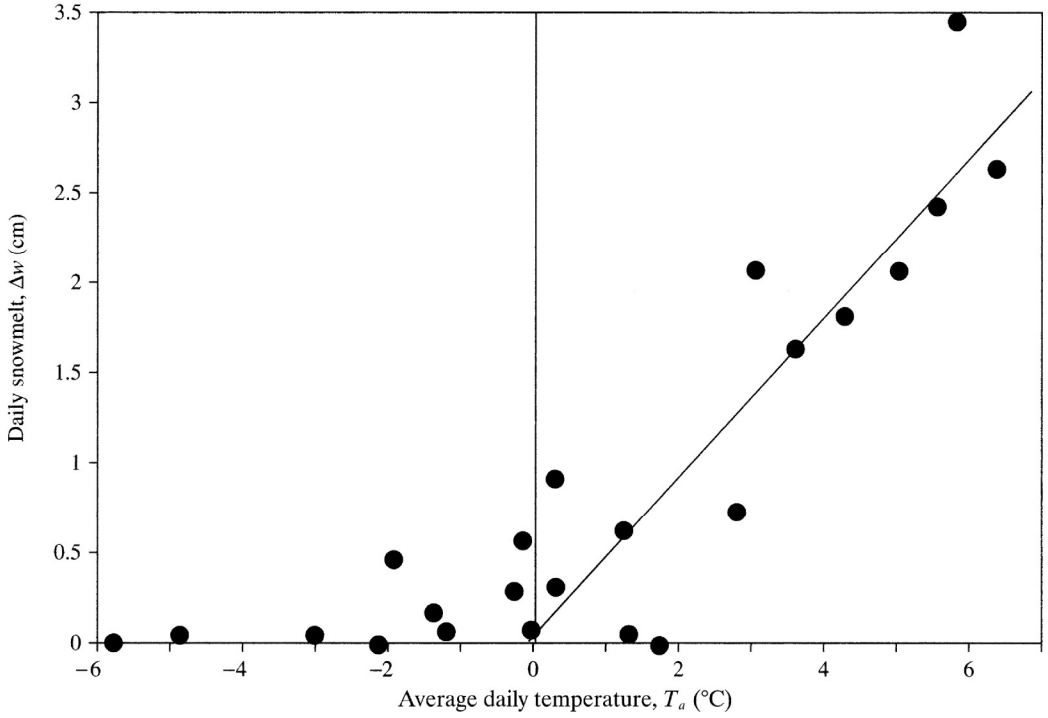

Figure 5.31 Daily snowmelt, Δw, as a function of daily average air temperature, T_a, at Danville, Vermont, March 1973. The line is the best-fit linear relation between the two variables for days when $T_a > 0$°C [data from Anderson et al. (1977)].

Table 5.7 General Melt-Factor Equations.

Male and Gray (1981)

$M = 4.0 \cdot (1 - a) \cdot \exp(-4 \cdot F) \cdot f_{sl}$

Federer and Lash (1978a) (forests in the eastern United States)

$M = f_F \cdot (0.7 + 0.0088 \cdot J) \cdot f_{sl}$, $J < 183$

Kuusisto (1986)

Forest: $M = 10.4 \cdot \frac{\rho_s}{\rho_w} - 0.7$;

Open: $M = 19.6 \cdot \frac{\rho_s}{\rho_w} - 2.39$

Symbols

$M \equiv$ melt factor (mm/C° · day)

$a \equiv$ albedo

$F \equiv$ fraction of forest cover

$f_{sl} \equiv$ **slope factor** ≡ ratio of solar radiation received on the site of interest to that on a horizontal surface [equation (D.27); a function of latitude, day-of-year, slope inclination, and slope aspect]

$f_F \equiv$ vegetative-cover factor = 30.0 for open areas, 17.5 for hardwood forests, and 10.0 for conifer forests

$J \equiv$ day-of-year ("Julian date")

$\rho_s \equiv$ snow density (kg/m^3)

$\rho_w \equiv$ water density (= 1,000 kg/m^3)

al. (1996) evaluated an approach that computes daily snowmelt, Δw, as

$$\Delta w = \frac{K + L}{\rho_w \cdot \lambda_f} + M_r \cdot T_a, \qquad \textbf{(5.72)}$$

where M_r is a "restricted" melt factor with a constant value of 2.0 mm/°C · d and T_a is average daily temperature (°C). In this method the radiation terms are measured or evaluated as described in sections 5.5.2.1 and 5.5.2.2, and M_r accounts for the turbulent-exchange processes. Brubaker et al. (1996) showed that the value of $M_r \approx 2.0$ mm/°C · d can be derived from the basic equations for those processes.

5.7.3 Evaluation of Snowmelt Models

Anderson (1976) made a thorough comparison of point energy-balance and temperature-index models with measured snowpack properties and snowmelt production over six snow seasons at the Danville, Vermont, research site. His complete model included simulation of snowpack settling and compaction as well as the snowpack energy balance, and was used for both accumulation and melt seasons. The temperature-index model, calibrated for the Danville site, is applicable only for the output phase of the melt season. Figure 5.32 compares snow-

course measurements of snowpack water equivalent and density with values simulated by Anderson's complete energy-balance model for the accumulation season and the warming and ripening phases of the melt season in 1972–1973. Figure 5.33 shows the same comparison for the output phase, and includes the predictions of the temperature-index model. Computed daily water output is compared with values measured in a lysimeter in figure 5.34. Clearly, both models perform very well in simulating density and water equivalent for the 1972–1973 snow season; this was true also in 1971–1972. In three of the other melt seasons examined, the energy-balance model gave somewhat better results, while the temperature-index model was slightly better during one season. Except for two of the highest-output days, predictions of water output were also good.

Figure 5.35 on p. 249 compares streamflow from a small (8.42 km^2) watershed at the Danville site with flow predicted with a model called the Snowmelt Runoff Model (SRM) (Brubaker et al. 1996) for six seasons. Two versions of the SRM are compared, one with melt predicted by the seasonally varying temperature-index approach [equation (5.71)], and the other with the hybrid approach [equation (5.72)]. The hybrid approach predicted daily runoff better in only two of the six years, but predicted total runoff volume significantly better in all years.

Kustas et al. (1994) compared lysimeter-measured snowmelt with melt estimated via (1) a complete energy balance, (2) the temperature-index approach with a seasonally increasing melt coefficient, and (3) the hybrid approach with radiation terms estimated as in sections 5.5.2.1 and 5.5.2.2 for a research site in Switzerland (figure 5.36 on p. 250). The accuracy of the hybrid approach was almost identical to that of the complete energy balance, and both were considerably better than the temperature-index estimates.

Anderson (1976) concluded that in heavily forested watersheds, a temperature-index model that includes a way to account for decreases in areal snow cover during melt should give results similar to an energy-balance model. However, an energy-balance model should perform better than a temperature-index model when applied to a relatively open (unforested) watershed where there is considerable variability in meteorological conditions, and in watersheds with considerable physiographic and climatic

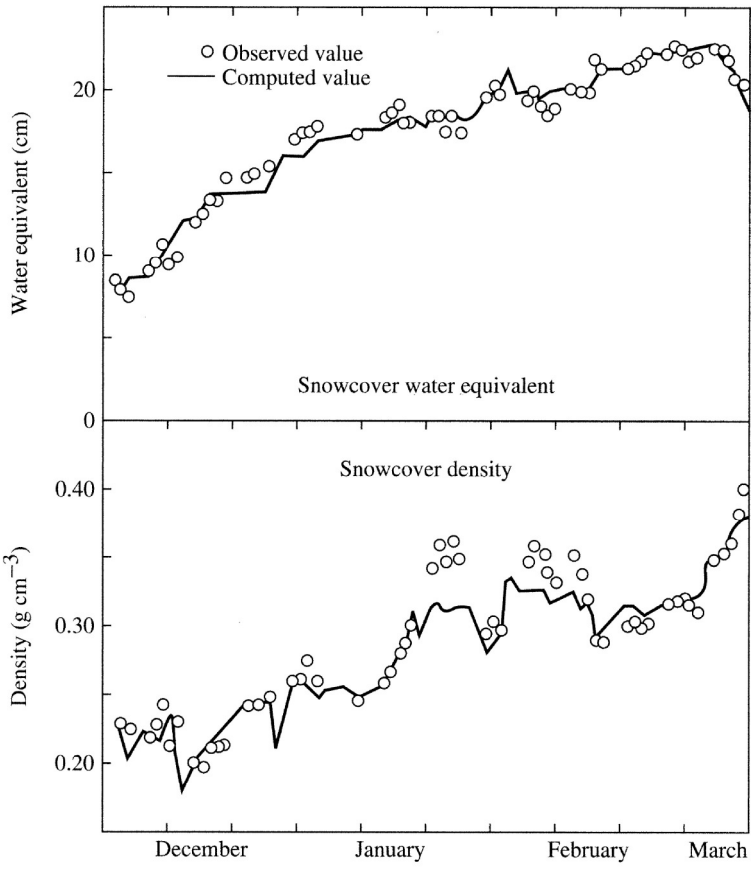

Figure 5.32 Comparison of observed and simulated (energy-balance model) snowpack water equivalent and density for the 1972–1973 accumulation season and warming and ripening phases of the melt season at Danville, Vermont. Observed values are snow-course observations [Anderson (1976)].

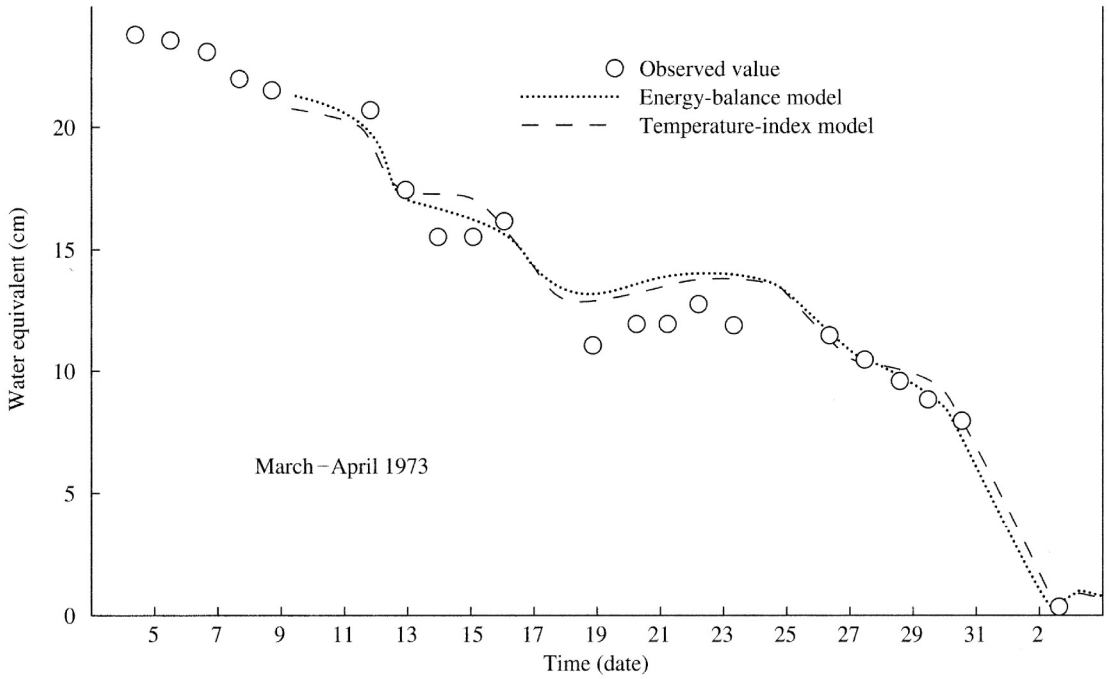

Figure 5.33 Comparison of observed and simulated (energy-balance and temperature-index models) snowpack water equivalent for the output phase of the 1973 melt season at Danville, Vermont. Observed values are snow-course observations [Anderson (1976)].

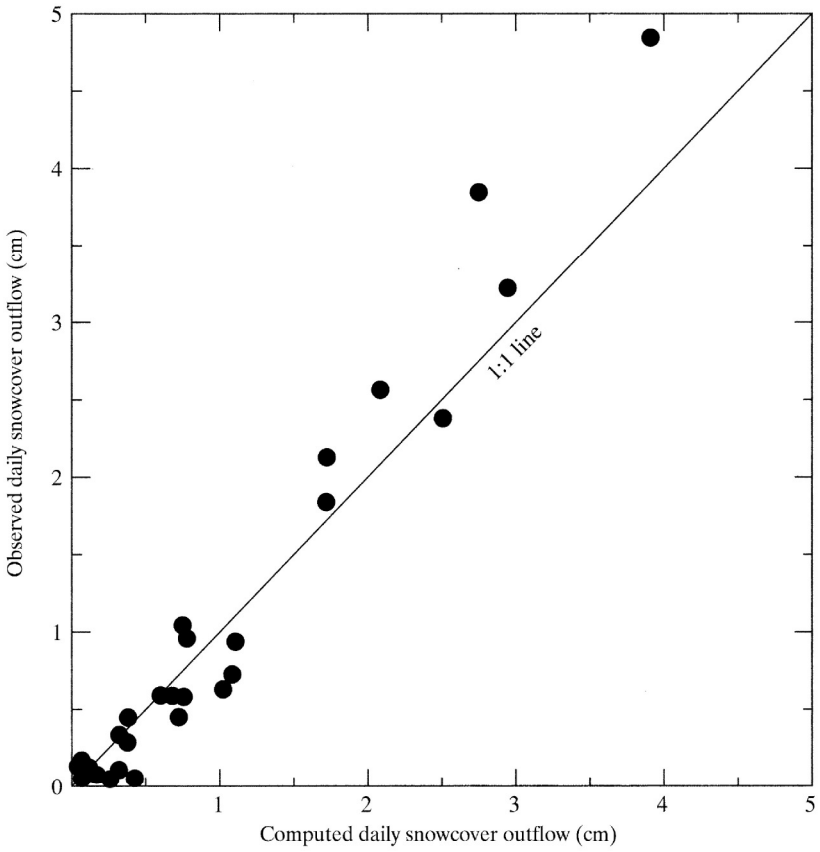

Figure 5.34 Water output observed in lysimeter versus simulated via energy-balance model at Danville, Vermont [Anderson (1976)].

variability. He found that the minimal data requirements for use of an energy-balance model are an accurate and representative estimate of incoming solar radiation, plus measurements of air temperature, vapor pressure, and wind speed.

Promising approaches to snowmelt that would be especially useful in predicting the effects of global warming on snow and snowmelt runoff include: (1) a model of the areal depletion of snow cover in a forested catchment (Buttle and McDonnell 1987), (2) a model that simulates the growth and disappearance of the seasonal snow cover from daily air temperature and precipitation data (Motoyama 1990), and (3) a model that uses areally averaged versions of the basic

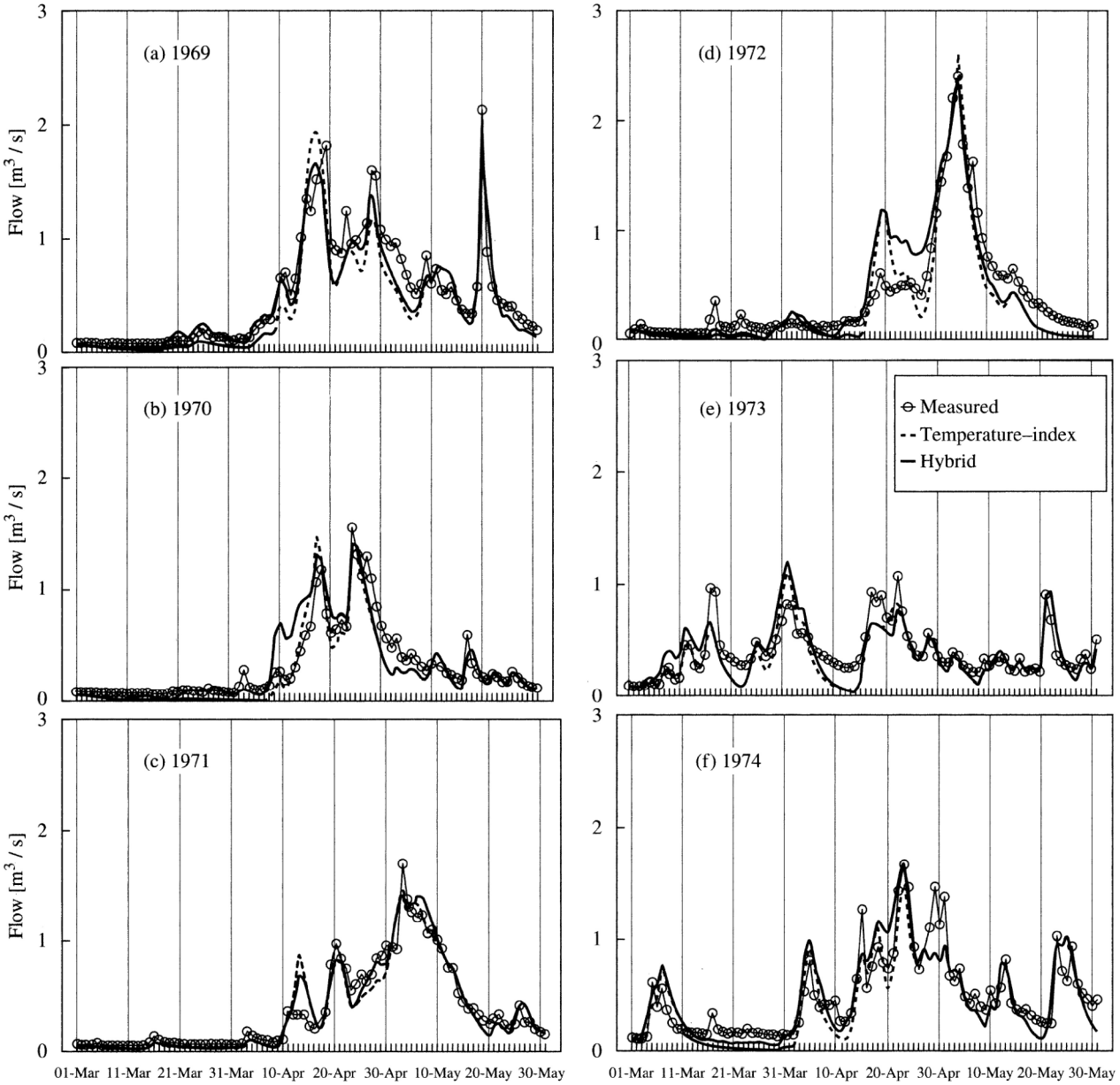

Figure 5.35 1969–1974 snowmelt runoff hydrographs at Sleepers River Research Watershed, Vermont. Open circles = measured; dashed line = modeled via temperature-index approach; solid line = modeled via hybrid approach [Brubaker et al. (1996). Incorporating radiation inputs into the Snowmelt Runoff Model. *Hydrological Processes* 10:1329–1343, with permission from Wiley].

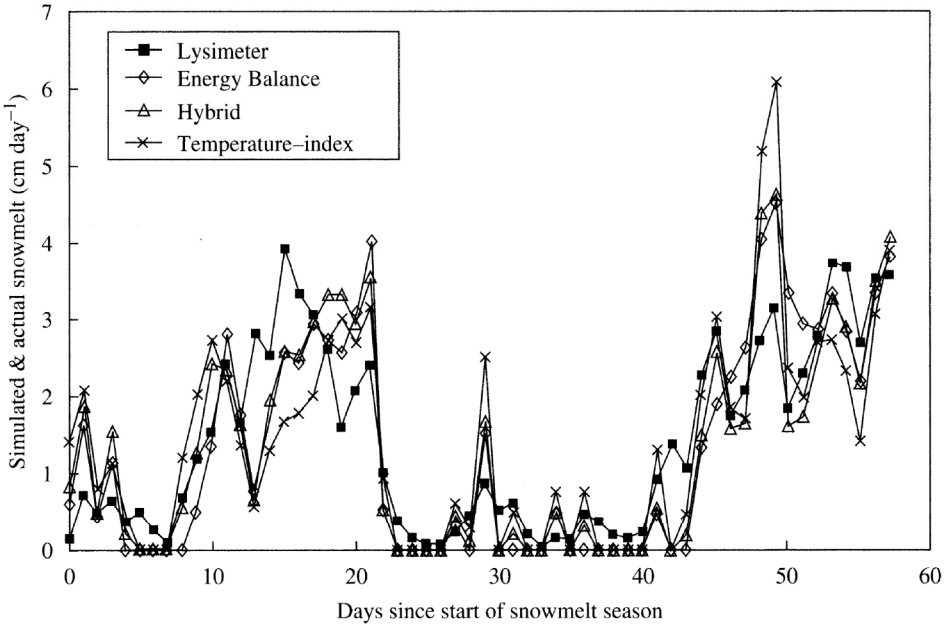

Figure 5.36 Daily snowmelt measured by lysimeter and simulated by the temperature-index approach, the hybrid approach, and the energy-balance approach at Weissfluhjoch, Switzerland, for the 1985 melt season [Kustas et al. (1994). A simple energy budget algorithm for the snowmelt runoff model. *Water Resources Research* 30:1515–1527, with permission of the American Geophysical Union].

energy-balance relations to predict areal snow cover and snowmelt runoff (Horne and Kavvas 1997).

The World Meteorological Organization (1986a) compared 11 temperature-index models using common data sets for six different watersheds, and other model comparisons were reported by Rango and Martinec (1994) and Blöschl et al. (1991a, 1991b). Rutter et al. (2009) evaluated 33 snowpack models of varying complexity and purpose across a wide range of hydrometeorological and forest-canopy conditions at five Northern Hemisphere locations, and compared modeled estimates of snow water equivalent or depth to observations at forest and open sites at each location. They found a great deal of variability in model performance from year to year and site to site, and concluded that there is no universal "best" model for all sites or locations.

5.7.4 Summary

Snowmelt is a significant contributor to runoff and water supplies over much of the Northern Hemisphere, and changes in snowmelt runoff will be one of the most pronounced hydrologic responses to global warming. Thus it is important that the processes of snow accumulation and melt are accurately captured in land-surface models. Many agencies have developed models that are specifically designed for particular regions, data sources, and purposes. However, they all attempt to simulate melt processes on the basis of meteorological data to account for the typically wide range of topography, land use, and weather over watersheds, and to integrate the processes of water movement over hillslopes and in stream channels. Because of the wide variability of conditions, the sparseness of surface meteorological data, and the need to provide operational forecasts at relatively short time intervals (usually less than 24 hr), some of these models use semi-empirical relations rather than physically based models of melt and water movement. Many watershed-scale models use some form of temperature-index model or hybrid approach to predict melt.

These results lead to the following conclusions:

- The understanding of snowpack processes as developed in sections 5.5 and 5.6 can be used to simulate point snowmelt to a high degree of precision given careful measurements of the meteorological inputs at the point of interest.
- The temperature-index approach can provide useful estimates of daily snowmelt, but the value of the melt coefficient should reflect local conditions and seasonal changes.
- The hybrid approach appears to predict daily snowmelt with a precision equivalent to the complete energy balance and, since good estimates of the radiation components of the energy balance can usually be made with commonly available data, this approach will often be attractive for modeling.

However, recent reviews of approaches to modeling snow processes (Roesch 2006; Andreadis et al.

2009; Parajka et al. 2010b; Rutter et al. 2009) have noted that the representation of snow processes in land-surface models is a key area in which improvements are required. Part of the difficulty arises because the physics of snow accumulation and ablation operate at much finer temporal and spatial scales than those resolved in most models. This problem is particularly important in mountainous areas, where orographic effects influence local precipitation, and in forested areas, where the canopy affects all aspects of the energy balance in complex ways.

Important challenges in modeling snowmelt over large areas remain, including:

- Accounting for differences in snow accumulation and melt over the typically large range of variations in topography, elevation, and vegetation.
- Achieving the correct partitioning of rain/snow (section 4.1.8). This problem is exacerbated in watersheds that have a wide range of elevation.
- Accounting for spatial and temporal variations in the areal extent of snow cover. Improvements in the interpretation of satellite imagery are evolving and will improve the estimation of areal snow cover (Dozier 2011).
- Accounting for the movement of water output to the watershed outlet. Empirical and semi-empirical techniques, some of which are discussed in chapter 10, are used for this.

▼ EXERCISES

1. Snow surveyors using a snow tube and thermometer recorded the following data from a snow course on two different dates (temperature was taken at the mid-point of the snow depth to represent the average snowpack temperature):

2 March 2013	Station 1	Station 2	Station 3	Station 4	Station 5
Depth (cm)	92	94	105	93	96
Water equivalent (cm)	29	30	33	29	32
Temperature (°C)	–6	–5	–6	–6	–6

7 March 2013	Station 1	Station 2	Station 3	Station 4	Station 5
Depth (cm)	88	89	102	88	91
Water equivalent (cm)	35	36	40	35	37
Temperature (°C)	–2	–2	–3	–2	–3

   a. Compute the snow density and cold content for both dates.
   b. How much energy needs to be added to the snowpack before water output begins?

2. The following snow-tube and temperature data were collected at five stations spaced 30 m apart on the University of New Hampshire baseball field:

31 January 2005	Station 1	Station 2	Station 3	Station 4	Station 5
Depth (cm)	20.1	18.3	18.2	16.4	24.5
Water equivalent (cm)	4.0	2.0	3.0	3.5	4.5
Temperature (°C)	0.0	0.0	0.0	0.0	–1.0

   At station 3, an undisturbed sample of snow measuring 33 cm wide by 50 cm long by 18.2 cm deep was collected in a plastic container with an empty weight of 1,284 g. The weight of the container with snow was 6,246 g.

   a. Calculate the average depth, density, and water equivalent of the snowpack.
   b. Compare the average density calculated from the snow tube with that calculated from the bulk sample.